Wave interaction with a large number of ice floes of arbitrary shapes

Yifeng Yang and Guoxiong Wu*
Department of Mechanical Engineering, University College London, Torrington Place, London WC1E 7JE, United Kingdom

(Received 7 September 2025; accepted 14 November 2025; published 12 December 2025)

Water wave interaction with a large number of floes is investigated, based on the linearized velocity potential theory for fluid flow, and elastic thin plate theory for ice floes. The solution procedure starts from a domain decomposition approach, and equations for velocity potentials are constructed via the boundary integral method in the free-surface and ice-covered subdomains, separately. The velocity potentials and normal velocities at the interface of different domains are expressed in terms of eigenfunction expansions in the vertical direction. This allows the three-dimensional equation to be reduced to a set of two-dimensional ones. Continuity of velocity and pressure are then imposed at the interface. A formula for evaluating hydrodynamic forces is derived, which requires only the results on the floe edge. When the number of ice floes becomes large, an efficient scheme is introduced to reduce computational effort, while the desired accuracy is maintained. The procedure is applicable to ice floes of arbitrary shapes and arrangements. Case studies are conducted for single and double arrays of circular and elliptical ice floes. Extensive results are provided for the hydrodynamic forces and far-field scattered wave energy. Their features and corresponding physics are discussed.

DOI: 10.1103/2r3s-16y4

I. INTRODUCTION

The Marginal Ice Zone (MIZ) is a transition area between the open ocean and regions covered by ice, which has been receiving increasing interest due to Arctic warming [1]. The MIZ is characterized by numerous floating ice floes, and their interaction with ocean surface waves plays a critical role in governing wave attenuation, energy dissipation, and potentially breakup of ice sheets. Therefore, from the perspectives of geophysical modeling, environmental protection, and Arctic maritime safety, it is essential to understand the physics of wave–ice floe interactions, which becomes ever more important as activities such as shipping and resource exploration become more frequent in these regions [2].

Over the past few decades, the problem of interaction between water waves and ice floes has been extensively studied using linearized velocity potential theory for the fluid flow and elastic thin plate theory for the ice sheet deformation [3], when its horizontal dimension is much larger than the vertical one. For typical three-dimensional (3D) problems, Meylan and Squire [4] studied the hydroelastic response of a circular ice floe floating on fluid of infinite depth. In their work, the boundary element method (BEM) with the Green's function satisfying the free-surface boundary

*Contact author: g.wu@ucl.ac.uk

condition was employed to find the velocity potential and the floe deformation numerically. Peter, Meylan, and Chung [5] considered the same problem in finite water depth and used a semianalytical solution procedure. In their work, the velocity potential was expanded into two separate double series along the circumferential and vertical directions: one for the fluid domain beneath the ice floe and the other for the free-surface region. These series were then matched at the interface to ensure continuity. Later, Montiel *et al.* [6] further considered the draught effect of a floating circular ice floe, and solved the problem using the matched eigenfunction expansion (MEE) approach. Their model was further verified by wave basin experiments. Meylan and Bennetts [7] studied the time-domain scattering of waves by a circular ice floe, where the time-domain solution is constructed from the frequency-domain solution of a circular ice floe. Apart from circular ice floes, recently several semianalytical approaches have been used to address the wave interaction problem with floating rectangular elastic plates. In particular, Porter [8] adopted a hybrid method combining the Fourier transform and the Rayleigh-Ritz technique. Ren, Wu, and Yang [9] further used an approach based on the Green's function to investigate surface wave interaction with a rectangular elastic plate floating in a channel. For ice floes of more general shapes, numerical approaches are usually required to solve the problems. For example, Meylan [10] investigated wave scattering by an ice floe of arbitrary geometry in infinite water depth. The solution was obtained using a boundary integral equation with the free-surface Green's function [11], while the ice floe displacement was represented through an approximate mode expansion. Later, Wang and Meylan [12] considered the same problem in finite water depth using a coupled numerical scheme. In particularly, the fluid flow problems were solved through the BEM, while the equations for elastic plates were dealt with using the finite element method (FEM). Later, Bennetts and Williams [13] investigated the wave scattering by an ice floe or a polynya of arbitrary smooth shapes. In their work, they first applied the vertical eigenfunction expansion to the velocity potential, which generated a system of two-dimensional Helmholtz equations. These equations were then converted to integro-differential equations using the Green's theorem and solved numerically via the Galerkin technique.

A large number of ice floes are usually present in real MIZs, and to have a good understanding of how water waves interact with multiple floating ice floes is highly relevant. Typically, Peter and Meylan [14] extended the procedure in Ref. [10] to multiple ice floes in infinite water depth. Bennetts and Squire [15] studied wave scattering by multiple ice floes arranged in a finite number of parallel strips, with each strip containing an infinite number of identical and evenly spaced floes. To solve the problem, they applied the periodic boundary conditions in each ice floe column, and expressed the velocity potential as a double series expansion, similar to the approach of Peter *et al.* [5]. Later, Montiel *et al.* [16] extended this procedure to model multiple parallel strips, each containing an infinite number of circular ice floes with prescribed statistical distributions in size and spatial location. In addition to works treating an infinite number of ice floes, Shi *et al.* [17] investigated the two-dimensional (2D) problem of wave transmission and reflection by multiple polynyas formed between finite-sized floating ice floes. To deal with cases involving a significant number of ice floes, they adopted an efficient wide-spacing approximation method to solve the problem with significantly reduced computational effort. More recently, Montiel *et al.* [18] considered wave scattering by an array of circular floating ice floes randomly distributed within a circular region. In their work, the fast multipole method (FMM) [19] was implemented to approximate and accelerate the evaluation of multiple interactions among the ice floes.

As discussed in Ref. [20], modeling wave scattering by multiple floating ice floes involves two main challenges. One is to efficiently simulate interactions among a large number of floes, and the other is to accurately represent floes with arbitrary shapes. Although a number of studies have been proposed to address wave scattering by single or a number of ice floes of arbitrary shapes [8,9,13], the most recent works on multiple ice floes mentioned above predominantly focus on floes with circular geometry. To address this limitation, the present paper employs a hybrid approach for modeling wave scattering by a large number of ice floes of arbitrary shapes. The velocity potentials in the free-surface and ice-covered domains are first constructed using the boundary integral equation, with the velocity potential and normal velocity at their interface expressed

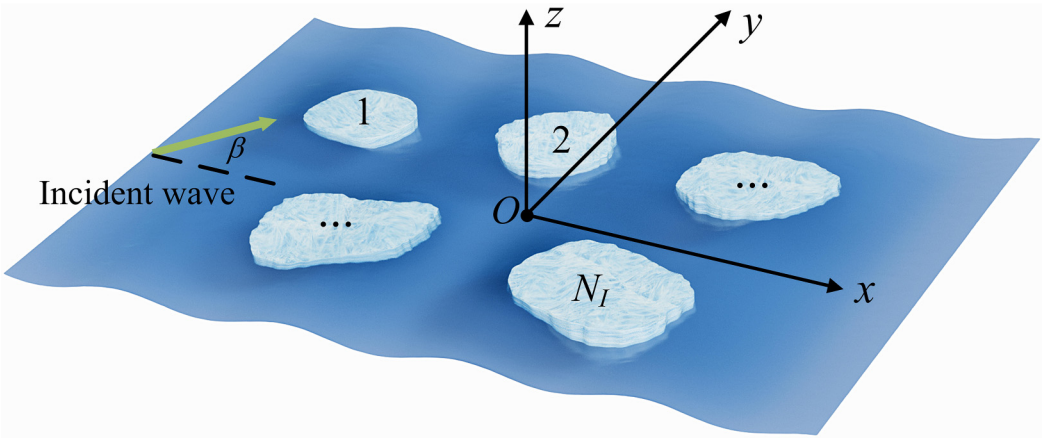

FIG. 1. Sketch of wave interaction with a large number of floating ice floes.

as eigenfunction series in the vertical direction. This formulation converts the three-dimensional boundary integral equations into an infinite set of two-dimensional ones in the horizontal plane. Continuity of pressure and normal velocity are then applied at each interface. Furthermore, when the number of ice floes becomes very large, an efficient computational approach is adopted to reduce the computational effort while the desired accuracy is maintained. Case studies are conducted for circular and elliptical ice floes of various configurations. Based on the numerical results, extensive analyses are carried out on the hydrodynamic forces acting on the floes and the diffracted wave energy at far field.

The rest of the paper is organized as follows. The mathematical model is established in Sec. II. The velocity potentials in the fluid domain with an ice cover and free-surface domain are established in Secs. III A and III B, respectively, followed by the procedure to match the velocity potentials and normal velocities at each interface of the two domains in Sec. III C. In Sec. III D, formulas to calculate the hydrodynamic forces on ice floes are derived. In Sec. III E, the far-field behavior of the solution is discussed. To address cases with a large number of ice floes, an efficient computational approach is described in Sec. III F. The numerical results and discussions are presented in Sec. IV, followed by the conclusions in Sec. V.

II. MATHEMATICAL FORMULATION

The problem of wave interaction with multiple ice floes of arbitrary shapes is sketched in Fig. 1. The ice floes are numbered $i = 1, \ldots, N_I$, where N_I represents the total number of ice floes. Each ice floe is assumed to have homogeneous physical properties, with density ρ_i, thickness h_i, Young's modulus E_i, and Poisson's ratio ν_i. To describe the problem, a Cartesian coordinate system $Oxyz$ is established, in which the origin is located at the mean water surface, the x and y axes are along the transverse plane, and the axis points upward. The seabed is assumed to be flat and along $z = -H$. An incident wave propagates along a direction with an angle of β to the positive x axis, and is disturbed by the ice floes.

It is assumed that the fluid with density ρ is homogeneous, inviscid, and incompressible, and its motion is irrotational. Thus, the velocity potential theory is adopted to describe the fluid flow. When the amplitude of wave motion is small compared to its wavelength, linearization can be further introduced to the boundary conditions. For a sinusoidal wave in time with frequency ω, we may write the total velocity potential Φ as

$$\Phi(x, y, z, t) = \mathrm{Re}\{\phi(x, y, z)e^{i\omega t}\}, \tag{1}$$

where ϕ is due to the incident, diffracted, and radiated waves. The potential satisfies the Laplace equation throughout the entire fluid domain,

$$\nabla^2\phi + \frac{\partial^2\phi}{\partial z^2} = 0, \quad -\infty < x, y < +\infty, \quad -H \leqslant z \leqslant 0, \tag{2}$$

where ∇^2 denotes the two-dimensional Laplacian in the Oxy plane.

It is assumed that all the ice floes float on the mean water surface with the draught effect neglected, and there is no gap between the lower surface of each ice floe and the upper water surface. Hence, the boundary conditions are imposed at the interface at $z = 0$. We may model each ice floe as an elastic thin plate [21]; the combined kinematic and dynamic boundary conditions give

$$(L_i\nabla^4 - m_i\omega^2 + \rho g)\frac{\partial\phi}{\partial z} - \rho\omega^2\phi = 0, \quad (x, y) \in S_i, \ z = 0, \tag{3}$$

where $L_i = E_i h_i^3/[12(1-\nu_i^2)]$ and $m_i = \rho_i h_i$ denote the flexural rigidity and mass per unit area of the ith ice floe ($i = 1, \ldots, N_I$), respectively, and S_i represents its lower surface. g is the acceleration due to gravity. In the free-surface region, the combined kinematic and dynamic boundary condition provides

$$g\frac{\partial\phi}{\partial z} - \omega^2\phi = 0, \quad (x, y) \notin \bigcup_{i=1}^{N_I} S_i, \quad z = 0. \tag{4}$$

On the seabed, the impermeable boundary condition is given as

$$\frac{\partial\phi}{\partial z} = 0, \quad z = -H. \tag{5}$$

The edge of each ice floe is assumed to be free to move, which requires zero bending moment and zero shear force conditions to be imposed, or

$$\begin{cases} \boldsymbol{\mathcal{B}}\left(\frac{\partial\phi}{\partial z}\right) = 0, \\ \boldsymbol{\mathcal{S}}\left(\frac{\partial\phi}{\partial z}\right) = 0, \end{cases} \quad (x, y) \in \Gamma_i, \quad z = 0, \tag{6a,b}$$

where $\Gamma_i = (x(s), y(s), 0)$ denotes the edge of surface S_i, and s is the curvilinear coordinate along the edge Γ_i, as also illustrated in Fig. 1. $\boldsymbol{\mathcal{B}}$ and $\boldsymbol{\mathcal{S}}$ in Eq. (6) represent the bending moment and shear force operators, respectively, and can be written as

$$\boldsymbol{\mathcal{B}} = \nabla^2 - \nu'_i\left(\frac{\partial^2}{\partial s^2} + \frac{\partial\Theta}{\partial s}\frac{\partial}{\partial n}\right), \tag{7a}$$

$$\boldsymbol{\mathcal{S}} = \frac{\partial}{\partial n}\nabla^2 + \nu'_i\frac{\partial}{\partial s}\left(\frac{\partial^2}{\partial s\partial n} - \frac{\partial\Theta}{\partial s}\frac{\partial}{\partial s}\right), \tag{7b}$$

where $\nu_i' = 1 - \nu_i$, and $\boldsymbol{n} = (\cos\Theta, \sin\Theta)$, and $\boldsymbol{s} = (-\sin\Theta, \cos\Theta)$ denote the unit outward normal and anticlockwise tangential vectors of Γ_i respectively, Θ is the angle between $\boldsymbol{n}$ and the x axis. Apart from all the conditions above, the following far-field condition is imposed to ensure waves propagating outward:

$$\lim_{r\to+\infty}\sqrt{r}\left(\frac{\partial}{\partial r} + \mathrm{i}k_0\right)(\phi - \phi_I) = 0, \tag{8}$$

where $r = \sqrt{x^2 + y^2}$, ϕ_I denotes the incident component of the velocity potential, and k_0 denotes the wave number of the propagating water wave and is the purely positive real root of the dispersion equation $K_w(k_0, \omega) = 0$ in the open water region, with

$$K_w(k, \omega) \equiv kg\tanh(kH) - \omega^2. \tag{9}$$

III. SOLUTION PROCEDURE

The domain decomposition approach is used to obtain the solution where two different types of fluid subdomains are defined, namely, $\Omega_i^{(\mathrm{I})}$ $(i = 1, \ldots, N_I)$, which represents the fluid domain beneath the ith ice cover, and $\Omega^{(\mathrm{II})}$, which denotes the free-surface fluid domain. In $\Omega_i^{(\mathrm{I})}$, we may write the velocity potential as $\phi_i^{(\mathrm{I})}$. In $\Omega^{(\mathrm{II})}$, the velocity potential is written as $\phi^{(\mathrm{II})} = \phi_I + \phi_D$, where ϕ_D represents the velocity potential of disturbed waves, comprising both the diffracted and radiated components. In both subdomains, $\phi_i^{(\mathrm{I})}$ and ϕ_D are constructed from the boundary integral equations first, and then the total velocity potentials are matched through the continuity conditions of the velocity potential and the normal velocity at each interface.

A. The velocity potential in the fluid domain with an ice cover

To construct $\phi_i^{(\mathrm{I})}$ in $\Omega_i^{(\mathrm{I})}$, we may use the boundary integral equation [22],

$$\Lambda^{(\mathrm{I})}(\boldsymbol{P})\phi_i^{(\mathrm{I})}(\boldsymbol{P}) = \int_{\Gamma_i} \left[\left\langle \phi_i^{(\mathrm{I})}(\boldsymbol{Q}), \frac{\partial G_i(\boldsymbol{P},\boldsymbol{Q})}{\partial n_0} \right\rangle - \left\langle G_i(\boldsymbol{P},\boldsymbol{Q}), \frac{\partial \phi_i^{(\mathrm{I})}(\boldsymbol{Q})}{\partial n_0} \right\rangle \right] \mathrm{d}s_0 \quad (i = 1, \ldots, N_I), \tag{10}$$

where $\boldsymbol{P}(x, y, z)$ and $\boldsymbol{Q}(x_0, y_0, z_0)$ represent the field and source points, respectively; $\Lambda^{(\mathrm{I})}(\boldsymbol{P})$ is the three-dimensional solid angle at $\boldsymbol{P}$; and the subscript 0 in Eq. (10) means the operation corresponding to the source point $\boldsymbol{Q}$. The operator $\langle f, g\rangle$ is defined as

$$\langle f, g\rangle = \int_{-H}^{0} f(z_0)g(z_0)\mathrm{d}z_0 + \frac{L_i}{\rho\omega^2}\left(\frac{\mathrm{d}f}{\mathrm{d}z_0}\frac{\mathrm{d}^3 g}{\mathrm{d}z_0^3} + \frac{\mathrm{d}^3 f}{\mathrm{d}z_0^3}\frac{\mathrm{d}g}{\mathrm{d}z_0}\right)_{z_0=0}, \tag{11}$$

where z_0 is along the surface $S_c^{(i)}$ extended vertically from Γ_i to the seabed. $G_i(\boldsymbol{P}, \boldsymbol{Q})$ in Eq. (10) corresponds the Green's function [23]

$$G_i(\boldsymbol{P},\boldsymbol{Q}) = \pi \mathrm{i} \sum_{m=-2}^{+\infty} \frac{\psi_m^{(i)}(z)\psi_m^{(i)}(z_0)}{Q_m^{(i)}} \times \mathcal{H}_0^{(2)}\left(\kappa_m^{(i)} R\right), \tag{12}$$

where $\mathcal{H}_0^{(2)}$ denotes the zero-order Hankel function of the second kind, R is the distance between (x, y) and (x_0, y_0), and

$$\psi_m^{(i)}(z) = \frac{\cosh\left[\kappa_m^{(i)}(z + H)\right]}{\cosh\left(\kappa_m^{(i)} H\right)}, \tag{13}$$

$$Q_m^{(i)} = \frac{2\kappa_m^{(i)} H + \sinh\left(2\kappa_m^{(i)} H\right)}{4\kappa_m^{(i)}\cosh^2\left(\kappa_m^{(i)} H\right)} + \frac{2L_i {\kappa_m^{(i)}}^4}{\rho\omega^2}\tanh^2\left(\kappa_m^{(i)} H\right). \tag{14}$$

The $\kappa_m^{(i)}$ $(m = -2, -1, \ldots)$ in Eq. (12) are an infinite number of roots to the dispersion equation $K_I^{(i)}(k, \omega) = 0$, where

$$K_I^{(i)}(k, \omega) \equiv (L_i k^4 - m_i\omega^2 + \rho g)k\tanh(kH) - \rho\omega^2. \tag{15}$$

Specifically, $\kappa_0^{(i)}$ is a purely positive real root, $\kappa_{-1}^{(i)}$ and $\kappa_{-2}^{(i)}$ are two complex roots with negative imaginary parts, with $\kappa_{-1}^{(i)} = -\bar{\kappa}_{-2}^{(i)}$, where the overbar represents the complex conjugate, and $\kappa_m^{(i)}$ $(m = 1, 2, \ldots)$ are an infinite number of purely negative imaginary roots.

To establish the expression of $\phi_i^{(\mathrm{I})}$, $\phi_i^{(\mathrm{I})}$ and $\partial\phi_i^{(\mathrm{I})}/\partial n$ along interface $S_c^{(i)}$ are first expanded into the eigenfunction series of vertical modes as

$$\begin{cases} \phi_i^{(\mathrm{I})}(\boldsymbol{P}) = \sum_{m=-2}^{+\infty} \varphi_m^{(i)}(x, y)\psi_m^{(i)}(z), \\ \frac{\partial\phi_i^{(\mathrm{I})}(\boldsymbol{P})}{\partial n} = \sum_{m=-2}^{+\infty} \frac{\partial\varphi_m^{(i)}(x,y)}{\partial n}\psi_m^{(i)}(z), \end{cases} \quad \boldsymbol{P} \in S_c^{(i)}. \tag{16a,b}$$

Substituting Eqs. (12) and (16) into the right-hand side of Eq. (10), and invoking the orthogonal property of $\psi_m^{(i)}(z_0)$ [24], or

$$\left\langle \psi_m^{(i)}(z_0), \psi_{\tilde{m}}^{(i)}(z_0) \right\rangle = \delta_{m\tilde{m}} Q_m^{(i)}, \tag{17}$$

where $\delta_{m\tilde{m}}$ denotes the Kronecker delta function, provides

$$\Lambda^{(\mathrm{I})}(\boldsymbol{P})\phi_i^{(\mathrm{I})}(\boldsymbol{P}) = \pi \mathrm{i} \sum_{m=-2}^{+\infty} \psi_m^{(i)}(z) \times \int_{\Gamma_i} \left[\varphi_m^{(i)}(x_0, y_0) \frac{\partial \mathcal{H}_0^{(2)}\left(\kappa_m^{(i)} R\right)}{\partial n_0} - \mathcal{H}_0^{(2)}\left(\kappa_m^{(i)} R\right) \frac{\partial \varphi_m^{(i)}(x_0, y_0)}{\partial n_0} \right] \mathrm{d}s_0. \tag{18}$$

We may further let the field point $\boldsymbol{P}$ be located on $S_c^{(i)}$. Noticing the orthogonal property of $\psi_m^{(i)}(z)$ again, we have

$$\Lambda^{(\mathrm{I})}(\boldsymbol{P})\varphi_m^{(i)}(x, y) - \pi \mathrm{i} \int_{\Gamma_i} \left[\varphi_m^{(i)}(x_0, y_0) \frac{\partial \mathcal{H}_0^{(2)}\left(\kappa_m^{(i)} R\right)}{\partial n_0} - \mathcal{H}_0^{(2)}\left(\kappa_m^{(i)} R\right) \frac{\partial \varphi_m^{(i)}(x_0, y_0)}{\partial n_0} \right] \mathrm{d}s_0 = 0. \tag{19}$$

If we start from the 2D Helmholtz equation [25], use $\frac{\pi \mathrm{i}}{2} \mathcal{H}_0^{(2)}(\kappa_m^{(i)} R)$ as the Green's function, and let $\alpha^{(\mathrm{I})}(\boldsymbol{P}) = \Lambda^{(\mathrm{I})}(\boldsymbol{P})/2$ be the 2D solid angle, the result will be the same as the above equation. In Eq. (19), it can be seen that the boundary integral equation for each $\varphi_m^{(i)}$ is independent through using Eq. (17). It is worth mentioning that in Ref. [13] the vertical modes were expanded from $m = 0$ to $m = +\infty$, while functions related to modes κ_{-2} and κ_{-1} were written in terms of other modes and the equations for $\varphi_m^{(i)}$ ($m = 0, 1, \ldots$) were fully coupled. It should also be mentioned that, as Γ_i is a closed curve, $\mathcal{H}_0^{(2)}(\kappa_m^{(i)} R)$ may be replaced by the Bessel function of the second kind, $Y_0(\kappa_m^{(i)} R)$, as the Bessel function of the first kind, $J_0(\kappa_m^{(i)} R)$, has no singularity over the surface confined by Γ_i, and its contribution will be zero when the Green's identity is used.

B. The velocity potential in the free-surface domain

In the free-surface domain $\Omega^{(\mathrm{II})}$, the governing equation for ϕ_D can be converted to an integral equation over its boundary. When the boundary conditions on the free surface and seabed, and at infinity, are used, the integral equation is reduced to that over only the interfaces $S_c^{(i)}$ with all $\Omega_i^{(\mathrm{I})}$. This gives

$$\Lambda^{(\mathrm{II})}(\boldsymbol{P})\phi_D(\boldsymbol{P}) = \sum_{i=1}^{N_I} \int_{\Gamma_i} \int_{-H}^{0} \left[\phi_D(\boldsymbol{Q}) \frac{\partial G_w(\boldsymbol{P}, \boldsymbol{Q})}{\partial n_0} - G_w(\boldsymbol{P}, \boldsymbol{Q}), \frac{\partial \phi_D(\boldsymbol{Q})}{\partial n_0} \right] \mathrm{d}z \mathrm{d}s_0, \tag{20}$$

where $\Lambda^{(\mathrm{II})}$ denotes the 3D solid angle at $\boldsymbol{P}$, and $G_w(\boldsymbol{P}, \boldsymbol{Q})$ denotes the Green's function for the free-surface problem [26,27], which can be expressed in the form of a vertical eigenfunction expansion as

$$G_w(\boldsymbol{P}, \boldsymbol{Q}) = \pi \mathrm{i} \sum_{m=0}^{+\infty} \frac{Z_m(z) Z_m(z_0)}{P_m} \times \mathcal{H}_0^{(2)}(k_m R), \tag{21}$$

where

$$Z_m(z) = \frac{\cosh[k_m(z + H)]}{\cosh(k_m H)}, \tag{22}$$

$$P_m = \frac{2k_m H + \sinh(2k_m H)}{4k_m \cosh^2(k_m H)}, \tag{23}$$

where k_m ($m = 0, 1, \ldots$) are an infinite number of roots of the dispersion equation $K_w(k_m, \omega) = 0$ in Eq. (9). In particular, k_0 is a purely positive one, as mentioned previously, and k_m ($m = 1, 2, \ldots$)

are an infinite number of purely negative imaginary ones. Similar to Eq. (16), we may expand ϕ_D and $\partial\phi_D/\partial n$ at the interface $S_c^{(i)}$ through the vertical mode eigenfunctions

$$\begin{cases} \phi_D(\boldsymbol{P}) = \sum_{m=0}^{+\infty} \phi_m^{(i)}(x,y) Z_m(z), \\ \frac{\partial \phi_D(\boldsymbol{P})}{\partial n} = \sum_{m=0}^{+\infty} \frac{\partial \phi_m^{(i)}(x,y)}{\partial n} Z_m(z), \end{cases} \quad \boldsymbol{P} \in S_c^{(i)}. \tag{24a,b}$$

Substituting Eqs. (21) and (24) into the right-hand side of Eq. (20), and noticing

$$\int_{-H}^{0} Z_m(z_0) Z_{\tilde{m}}(z_0) \mathrm{d}z_0 = \delta_{m\tilde{m}} P_m, \tag{25}$$

we have

$$\Lambda^{(\mathrm{II})}(\boldsymbol{P})\phi_D(\boldsymbol{P}) = \pi \mathrm{i} \sum_{i=1}^{N_I} \sum_{m=0}^{+\infty} Z_m(z) \times \int_{\Gamma_i} \left[\phi_m^{(i)}(x_0,y_0) \frac{\partial \mathcal{H}_0^{(2)}(k_m R)}{\partial n_0} - \mathcal{H}_0^{(2)}(k_m R) \frac{\partial \phi_m^{(i)}(x_0,y_0)}{\partial n_0} \right] \mathrm{d}s_0. \tag{26}$$

Letting $\boldsymbol{P}$ be located on $S_c^{(i)}$ and using Eq. (24a) again, this provides

$$\Lambda^{(\mathrm{II})}(\boldsymbol{P})\phi_m^{(i)}(x,y) - \pi \mathrm{i} \sum_{i=1}^{N_I} \int_{\Gamma_i} \left[\phi_m^{(i)}(x_0,y_0) \frac{\partial \mathcal{H}_0^{(2)}(k_m R)}{\partial n_0} - \mathcal{H}_0^{(2)}(k_m R) \frac{\partial \phi_m^{(i)}(x_0,y_0)}{\partial n_0} \right] \mathrm{d}s_0 = 0. \tag{27}$$

It should be noted that $\Lambda^{(\mathrm{II})}(\boldsymbol{P})$ is the 3D solid angle. Similar to Eq. (19), Eq. (27) can also be established from the 2D Helmholtz equation, and $\alpha^{(\mathrm{II})}(\boldsymbol{P}) = \Lambda^{(\mathrm{II})}(\boldsymbol{P})/2$ will be the 2D solid angle. Besides, each mode in Eq. (27) at a given m is a dependent 2D equation. It is worth mentioning that, unlike Eq. (19), $\mathcal{H}_0^{(2)}(k_m R)$ in Eq. (27) cannot be replaced by $Y_0(k_m R)$, because the domain $\Omega^{(\mathrm{II})}$ tends to infinity and the latter does not satisfy the radiation condition.

The velocity potential ϕ_I of the incident wave can be written as

$$\phi_I(\boldsymbol{P}) = I Z_0(z) e^{-\mathrm{i}k_0(x\cos\beta + y\sin\beta)}, \tag{28}$$

where $I = Ag/\mathrm{i}\omega$, and A denotes the amplitude of the incident wave and β denotes the angle between the wave direction and the positive x axis, as mentioned above.

C. Matching of the solutions on interfaces of subdomains

On the interface $S_c^{(i)}$ between each ice cover and the free-surface domains, continuity conditions should be imposed on the velocity potential and its normal derivative, or

$$\begin{cases} \phi_i^{(\mathrm{I})}(\boldsymbol{P}) = \phi^{(\mathrm{II})}(\boldsymbol{P}), \\ \frac{\partial \phi_i^{(\mathrm{I})}(\boldsymbol{P})}{\partial n} = \frac{\partial \phi^{(\mathrm{II})}(\boldsymbol{P})}{\partial n}, \end{cases} \quad \boldsymbol{P} \in S_c^{(i)}. \tag{29a,b}$$

To achieve this, we may first apply the operator in Eq. (11) to $\phi_i^{(\mathrm{I})}(\boldsymbol{P})$ and $\psi_m^{(i)}(z)$, which gives

$$\begin{aligned} \left\langle \phi_i^{(\mathrm{I})}, \psi_m^{(i)} \right\rangle &= \int_{-H}^{0} \phi_i^{(\mathrm{I})} \psi_m^{(i)} \mathrm{d}z + \frac{L_i}{\rho\omega^2} \left[\frac{\partial \phi_i^{(\mathrm{I})}}{\partial z} \frac{\mathrm{d}^3 \psi_m^{(i)}}{\mathrm{d}z^3} + \frac{\partial^3 \phi_i^{(\mathrm{I})}}{\partial z^3} \frac{\mathrm{d}\psi_m^{(i)}}{\mathrm{d}z} \right]_{z=0} \\ &= \int_{-H}^{0} \phi^{(\mathrm{II})} \psi_m^{(i)} \mathrm{d}z + \frac{L_i}{\rho\omega^2} \left[\frac{\partial \phi_i^{(\mathrm{I})}}{\partial z} \frac{\mathrm{d}^3 \psi_m^{(i)}}{\mathrm{d}z^3} + \frac{\partial^3 \phi_i^{(\mathrm{I})}}{\partial z^3} \frac{\mathrm{d}\psi_m^{(i)}}{\mathrm{d}z} \right]_{z=0}, \quad \boldsymbol{P} \in S_c^{(i)}. \end{aligned} \tag{30}$$

Following the procedure in Ref. [28], we may introduce two unknown functions:

$$\begin{cases} \frac{\partial \phi_i^{(\mathrm{I})}(x,y,0)}{\partial z} = A_i(x,y), \\ \frac{\partial^3 \phi_i^{(\mathrm{I})}(x,y,0)}{\partial z^3} = B_i(x,y). \end{cases} \tag{31a,b}$$

Substituting Eqs. (16a), (24a), and (28) into Eq. (30), and invoking the orthogonal properties of $\psi_m^{(i)}$ in Eq. (17), we obtain

$$Q_m^{(i)}\varphi_m^{(i)}(x,y) - \sum_{\tilde{m}=0}^{+\infty} X\left(k_{\tilde{m}}, \kappa_m^{(i)}\right)\phi_{\tilde{m}}^{(i)}(x,y) - \frac{L_i\kappa_m^{(i)}\tanh\left(\kappa_m^{(i)}H\right)}{\rho\omega^2}\left[{\kappa_m^{(i)}}^2 A_i(x,y) + B_i(x,y)\right]$$
$$= IX\left(k_0, \kappa_m^{(i)}\right)e^{-\mathrm{i}k_0(x\cos\beta + y\sin\beta)}, \quad (x,y)\in\Gamma_i, \tag{32}$$

where

$$X(x_1,x_2) = \frac{x_1\tanh(x_1H) - x_2\tanh(x_2H)}{x_1^2 - x_2^2}. \tag{33}$$

To satisfy Eq. (29b), we may use

$$\int_{-H}^{0}\frac{\partial\phi^{(\mathrm{II})}}{\partial n}Z_m\mathrm{d}z = \int_{-H}^{0}\frac{\partial\phi_i^{(\mathrm{I})}}{\partial n}Z_m\mathrm{d}z, \quad \boldsymbol{P}\in S_c^{(i)}. \tag{34}$$

Applying Eqs. (16b), (24b), and (28) to Eq. (34), and using Eq. (25), we have

$$P_m\frac{\partial\phi_m^{(i)}(x,y)}{\partial n} - \sum_{\tilde{m}=-2}^{+\infty} X\left(\kappa_{\tilde{m}}^{(i)}, k_m\right)\frac{\partial\varphi_{\tilde{m}}^{(i)}(x,y)}{\partial n} = \delta_{m0}\mathrm{i}k_0P_0I(n_x\cos\beta + n_y\sin\beta)e^{-\mathrm{i}k_0(x\cos\beta+y\sin\beta)},$$
$$(x,y)\in\Gamma_i, \tag{35}$$

where $n_x = \cos\Theta$ and $n_y = \sin\Theta$ denote components of the unit normal vector at Γ_i. Apart from the conditions above, the edge conditions should also be imposed for each floe. We may apply Eqs. (6) and (7) to Eq. (16). This give

$$\sum_{m=-2}^{+\infty}\left[{\kappa_m^{(i)}}^2\varphi_m^{(i)}(x,y) + \nu_i'\left(\frac{\partial^2}{\partial s^2} + \frac{\partial\Theta}{\partial s}\frac{\partial}{\partial n}\right)\varphi_m^{(i)}(x,y)\right]\kappa_m^{(i)}\tanh\left(\kappa_m^{(i)}H\right) = 0, \quad (x,y)\in\Gamma_i, \tag{36a}$$

$$\sum_{m=-2}^{+\infty}\left[{\kappa_m^{(i)}}^2\frac{\partial\varphi_m^{(i)}(x,y)}{\partial n} - {\nu'}_i\frac{\partial}{\partial s}\left(\frac{\partial^2}{\partial s\partial n} - \frac{\partial\Theta}{\partial s}\frac{\partial}{\partial s}\right)\varphi_m^{(i)}(x,y)\right]\kappa_m^{(i)}\tanh\left(\kappa_m^{(i)}H\right) = 0, \quad (x,y)\in\Gamma_i. \tag{36b}$$

Before solving the established system of linear equations, we may combine Eqs. (19) and (32) to eliminate $\varphi_m^{(i)}$, which gives

$$\frac{\Lambda^{(\mathrm{I})}(\boldsymbol{P})}{Q_m^{(i)}}\left\{\sum_{\tilde{m}=0}^{+\infty}X\left(k_{\tilde{m}},\,\kappa_m^{(i)}\right)\phi_{\tilde{m}}^{(i)}(x,y) + \frac{L_i\kappa_m^{(i)}\tanh\left(\kappa_m^{(i)}H\right)}{\rho\omega^2}\left[{\kappa_m^{(i)}}^2A_i(x,y) + B_i(x,y)\right]\right\}$$
$$-\pi\mathrm{i}\int_{\Gamma_i}\left\{\frac{1}{Q_m^{(i)}}\left\{\sum_{\tilde{m}=0}^{+\infty}X\left(k_{\tilde{m}},\kappa_m^{(i)}\right)\phi_{\tilde{m}}^{(i)}(x_0,y_0) + \frac{L_i\kappa_m^{(i)}\tanh\left(\kappa_m^{(i)}H\right)}{\rho\omega^2}\left[{\kappa_m^{(i)}}^2A_i(x_0,y_0) + B_i(x_0,y_0)\right]\right\}\right.$$
$$\left.\times\frac{\partial\mathcal{H}_0^{(2)}\left(\kappa_m^{(i)}R\right)}{\partial n_0} - \mathcal{H}_0^{(2)}\left(\kappa_m^{(i)}R\right)\frac{\partial\varphi_m^{(i)}(x_0,y_0)}{\partial n_0}\right\}\mathrm{d}s_0$$
$$= \frac{IX\left(k_0,\kappa_m^{(i)}\right)}{Q_m^{(i)}}\left\{-\Lambda^{(\mathrm{I})}(\boldsymbol{P})e^{-ik_0(x\cos\beta+y\sin\beta)} + \pi\mathrm{i}\int_{\Gamma_i}e^{-\mathrm{i}k_0(x_0\cos\beta+y_0\sin\beta)}\frac{\partial\mathcal{H}_0^{(2)}\left(\kappa_m^{(i)}R\right)}{\partial n_0}\mathrm{d}s_0\right\}. \tag{37}$$

Similarly, combining Eqs. (27) and (35) to eliminate $\partial\phi_m^{(i)}/\partial n$, we obtain

$$\Lambda^{(\mathrm{II})}(\boldsymbol{P})\phi_m^{(i)}(x,y) - \pi \mathrm{i}\sum_{i=1}^{N_I}\int_{\Gamma_i}\left[\phi_m^{(i)}(x_0,y_0)\frac{\partial \mathcal{H}_0^{(2)}(k_mR)}{\partial n_0} - \frac{\mathcal{H}_0^{(2)}(k_mR)}{P_m}\right.$$
$$\left.\times\sum_{\tilde{m}=-2}^{+\infty} X\left(\kappa_{\tilde{m}}^{(i)},k_m\right)\frac{\partial\varphi_{\tilde{m}}^{(i)}(x_0,y_0)}{\partial n_0}\right]\mathrm{d}s_0$$
$$= \delta_{m0}\pi k_0 I\sum_{i=1}^{N_I}\int_{\Gamma_i}(n_{x_0}\cos\beta + n_{y_0}\sin\beta)e^{-\mathrm{i}k_0(x_0\cos\beta+y_0\sin\beta)}\mathcal{H}_0^{(2)}(k_mR)\mathrm{d}s_0. \tag{38}$$

During the numerical computation, the infinite series in Eqs. (16) and (24) are truncated at $m = M$. Each ice edge Γ_i $(i = 1,\ldots,N_I)$ is discretized as $N_s^{(i)}$ segments. In each segment, $\varphi_m^{(i)}$, $\partial\varphi_m^{(i)}/\partial n$, $\phi_m^{(i)}$, and $\partial\phi_m^{(i)}/\partial n$ are assumed to vary linearly along each segment. In such a case, the BEM with the linear element [29] can be used to solve Eqs. (37) and (38). Based on this discretization scheme, we totally have $(M+3)\sum_{i=1}^{N_I}N_s^{(i)}$ unknowns for $\partial\varphi_m^{(i)}/\partial n$, $(M+1)\sum_{i=1}^{N_I}N_s^{(i)}$ unknowns for $\phi_m^{(i)}$, as well as $2\sum_{i=1}^{N_I}N_s^{(i)}$ unknowns for A_i and B_i, respectively. Hence, there is a total of $2(M+3)\sum_{i=1}^{N_I}N_s^{(i)}$ unknowns. At the same time, Eqs. (37) and (38) provide $(M+3)\sum_{i=1}^{N_I}N_s^{(i)}$ and $(M+1)\sum_{i=1}^{N_I}N_s^{(i)}$ equations, and the edge conditions [Eqs. (36a) and (36b)] give the additional $2\sum_{i=1}^{N_I}N_s^{(i)}$ equations. Thus, the number of equations is the same as the number of unknowns. In Eq. (36), the derivatives with respect to s are numerically treated using a finite difference scheme [30].

D. Hydrodynamic forces on ice floes

Once all the unknowns are found, the hydrodynamic pressure $p^{(i)}$ on the ith ice floe can be obtained from the linear Bernoulli equation,

$$p^{(i)}(\boldsymbol{P}) = -\mathrm{i}\omega\rho\phi_i^{(\mathrm{I})}(\boldsymbol{P}) - \rho g\eta_i^{(\mathrm{I})}(\boldsymbol{P}), \quad z = 0, \tag{39}$$

where $\eta_i^{(\mathrm{I})} = \frac{1}{\mathrm{i}\omega}\frac{\partial\phi_i^{(\mathrm{I})}}{\partial z}$ denotes wave elevation or the ice sheet displacement including both rigid motion and elastic deflection corresponding to $\phi_i^{(\mathrm{I})}$. Hence, the hydrodynamic forces on the ith ice floe can be calculated from the integration of $p^{(i)}$ over the lower surface of the ice sheet, S_i, or

$$F_j^{(i)} = -\frac{\mathrm{i}\rho}{\omega}\iint_{S_i}\left[\omega^2\phi_i^{(\mathrm{I})}(\boldsymbol{P}) - g\frac{\partial\phi_i^{(\mathrm{I})}(\boldsymbol{P})}{\partial z}\right]N_j^{(i)}\mathrm{d}S, \tag{40}$$

where $j = 1,2,3$ correspond to the vertical heave force F_z, the roll (M_x), and the pitch (M_y) moments about the lines $x = x_c^{(i)}$ and $y = y_c^{(i)}$, respectively, $(N_1^{(i)}, N_2^{(i)}, N_3^{(i)}) = (1, y-y_c^{(i)}, x_c^{(i)} - x)$, and $(x_c^{(i)},\ y_c^{(i)})$ denotes the rotational center of the ith ice floe. We notice that the integral in Eq. (40) requires results of $\phi_i^{(\mathrm{I})}$ and $\partial\phi_i^{(\mathrm{I})}/\partial z$, while the solution of the system of linear equations in Sec. III C is only along the edge Γ_i. They can be obtained using Eq. (19) for each m. However, this would lead to a significant amount of additional computational effort. To avoid this, we may apply Eq. (3) to Eq. (40), which gives

$$F_j^{(i)} = F_{j,1}^{(i)} + F_{j,2}^{(i)}, \quad j = 1,2,3, \tag{41}$$

where

$$\begin{cases} F_{j,1}^{(i)} = \frac{L_i}{i\omega}\iint_{S_i}\nabla^4\left(\frac{\partial\phi_i^{(\mathrm{I})}}{\partial z}\right)N_j^{(i)}\mathrm{d}S, \\ F_{j,2}^{(i)} = \mathrm{i}m_i\omega\iint_{S_i}\frac{\partial\phi_i^{(\mathrm{I})}}{\partial z}N_j^{(i)}\mathrm{d}S, \end{cases} \tag{42a,b}$$

where $F_{j,1}^{(i)}$ and $F_{j,2}^{(i)}$ represent the components caused by bending and acceleration of the plate, respectively. We may apply the Gaussian theorem to Eq. (42a), which provides

$$F_{j,1}^{(i)} = \frac{L_i}{\mathrm{i}\omega}\int_{\Gamma_i}\left\{N_j^{(i)}\frac{\partial}{\partial n}\left[\nabla^2\left(\frac{\partial \phi_i^{(\mathrm{I})}}{\partial z}\right)\right] - \frac{\partial N_j^{(i)}}{\partial n}\nabla^2\left(\frac{\partial \phi_i^{(\mathrm{I})}}{\partial z}\right)\right\}\mathrm{d}s, \tag{43}$$

where $\partial/\partial n$ in Eq. (43) denotes the normal derivative of Γ_i, pointing outward, and $\partial N_j^{(i)}/\partial n = 0$, n_y, and $-n_x$ for $j = 1, 2, 3$, respectively. Applying the edge conditions in Eq. (7) to Eq. (43), we have

$$F_{j,1}^{(i)} = -\frac{\nu'_i L_i}{\mathrm{i}\omega}\int_{\Gamma_i}\left\{N_j^{(i)}\frac{\partial}{\partial s}\left(\frac{\partial^2}{\partial s \partial n} - \frac{\partial \Theta}{\partial s}\frac{\partial}{\partial s}\right)\frac{\partial \phi_i^{(\mathrm{I})}}{\partial z} + \frac{\partial N_j^{(i)}}{\partial n}\left(\frac{\partial^2}{\partial s^2} + \frac{\partial \Theta}{\partial s}\frac{\partial}{\partial n}\right)\frac{\partial \phi_i^{(\mathrm{I})}}{\partial z}\right\}\mathrm{d}s. \tag{44}$$

Using integration by parts, and noticing $\frac{\partial n_x}{\partial s} = -n_y\frac{\partial \Theta}{\partial s}$ and $\frac{\partial n_y}{\partial s} = n_x\frac{\partial \Theta}{\partial s}$, we obtain

$$F_{j,1}^{(i)} = 0. \tag{45}$$

This indicates that the bending of the plate does not contribute to the hydrodynamic forces, and there is only $F_{j,2}^{(i)}$. This is not a surprise, as this is in fact a term of integration of mass times acceleration. In the case of the free edge, there is no external loading. This term must be equal to the hydrodynamic force. Noticing that $\phi_i^{(\mathrm{I})}$ is governed by the Laplace equation in the internal fluid domain $\Omega_i^{(\mathrm{I})}$, the Green's second identity provides

$$\oiint_{S_i+S_c^{(i)}+S_b}\left[\frac{\partial \phi_i^{(\mathrm{I})}}{\partial n}N_j^{(i)} - \phi_i^{(\mathrm{I})}\frac{\partial N_j^{(i)}}{\partial n}\right]\mathrm{dS} = 0. \tag{46}$$

Invoking $\partial N_j^{(i)}/\partial z = 0$, and the impermeable condition on the seabed, S_b, the integration in Eq. (42b) over S_i can be converted to that over the interface $S_c^{(i)}$. This gives

$$F_{j,2}^{(i)} = -\mathrm{i}m_i\omega\iint_{S_c^{(i)}}\left[N_j^{(i)}\frac{\partial \phi_i^{(\mathrm{I})}}{\partial n} - \phi_i^{(\mathrm{I})}\frac{\partial N_j^{(i)}}{\partial n}\right]\mathrm{d}S. \tag{47}$$

Substituting Eqs. (16a) and (16b) into Eq. (47), and performing the integration along the z direction analytically, we obtain

$$F_j^{(i)} = F_{j,2}^{(i)} = -\mathrm{i}m_i\omega\sum_{m=-2}^{+\infty}\frac{\tanh\left(\kappa_m^{(i)}H\right)}{\kappa_m^{(i)}} \times \oint_{\Gamma_i}\left[N_j^{(i)}\frac{\partial \varphi_m^{(i)}}{\partial n} - \varphi_m^{(i)}\frac{\partial N_j^{(i)}}{\partial n}\right]\mathrm{d}s, \tag{48}$$

where only a line integral along Γ_i is involved.

E. Far-field behavior of the solution

The wave energy at the far field is an important indicator for how the incoming wave is scattered by the floating ice floes. To investigate that, we write the asymptotic expansion of the Hankel function at $r = \sqrt{x^2+y^2} \to +\infty$ as [31]

$$\mathcal{H}_0^{(2)}(k_m R) \approx \sqrt{\frac{2}{\pi k_m r}}e^{-\mathrm{i}\left(k_m r - \frac{\pi}{4}\right)}e^{\mathrm{i}k_m r_0\cos(\theta-\theta_0)}, \tag{49}$$

where $r_0 = \sqrt{x_0^2+y_0^2}$, $\tan\theta = y/x$, and $\tan\theta_0 = y_0/x_0$. Applying Eq. (49) to Eq. (26), keeping only the traveling wave term $m = 0$, and ignoring exponentially decaying terms, ϕ_D can be written as

$$\lim_{r\to+\infty}\phi_D(\boldsymbol{P}) = \sqrt{\frac{2}{\pi k_0 r}}U(\theta)Ie^{-\mathrm{i}\left(k_0 r - \frac{\pi}{4}\right)}Z_0(z), \tag{50}$$

where $U(\theta)$ denotes the diffraction coefficient and can be expressed as

$$U(\theta) = \frac{1}{4\mathrm{i}I}\sum_{i=1}^{N_I}\int_{\Gamma_i}\left[\phi_0^{(i)}(x_0, z_0)\frac{\partial f(x_0, z_0)}{\partial n_0} - f(x_0, z_0)\frac{\partial \phi_0^{(i)}(x_0, z_0)}{\partial n_0}\right]\mathrm{d}s_q, \tag{51}$$

and $f(x_0, z_0) = e^{\mathrm{i}k_0 r_0 \cos(\theta-\theta_0)}$. The scattering cross section,

$$\mathcal{F} = \frac{1}{2\pi}\int_{-\pi}^{\pi}|U(\theta)|^2\mathrm{d}\theta, \tag{52}$$

can be used as a measure of the diffracted wave energy. Alternatively, following Ref. [32], applying the Green's second identity to ϕ_D and its conjugate $\bar{\phi}_D$, using the far-field behavior of ϕ_D, as well as the method of the stationary phase, $\mathcal{F}$ can be also written as

$$\mathcal{F} = -\mathrm{Re}[U(\beta)]. \tag{53}$$

Equations (52) and (53) can be used to check and validate the numerical results.

It is worth mentioning that the total hydrodynamic forces on all the ice floes can be also linked to the velocity potential in the far field. We may first sum $F_{j,2}^{(i)}$ in Eq. (47) from $i = 1, \ldots, N_I$, and then apply the Green's second identity, which provides

$$\sum_{i=1}^{N_I}F_{j,2}^{(i)} = \mathrm{i}\omega\iint_{S_\infty}\left[\Psi_j\frac{\partial\phi^{(\mathrm{II})}}{\partial r} - \frac{\partial\Psi_\mathrm{j}}{\partial r}\phi^{(\mathrm{II})}\right]\mathrm{d}S, \quad j = 1, \ldots, 3, \tag{54}$$

where Ψ_j denotes the radiation velocity potential satisfying $\frac{\partial\Psi_j}{\partial n} = m_i N_j^{(i)}$ on $S_c^{(i)}$ $(i = 1, \ldots, N_I)$ in the free-surface wave problem, which can be derived based on the standard procedure in Ref. [26], S_∞ denotes the vertical circular surface at $r \to +\infty$. $\phi^{(\mathrm{II})} = \phi_I + \phi_D$ and introduction at the beginning of Sec. III.

F. An efficient iterative computational approach

In scenarios with a large number of floating ice floes, the stiffness matrix corresponding to the system of linear equations established by Eqs. (36)–(38) will be excessively large, which drastically increases the requirement for storage and time for computing if directly using conventional approaches, e.g., Gaussian elimination with pivot selection and lower-upper (LU) decomposition. In such a case, we may employ an efficient iteration method here. The matrix equation corresponding to the ith ice floe can be written as

$$\mathbf{A}_i\mathbf{\Phi}_i = \mathbf{B}_i - \sum_{\substack{j=1\\ j\neq i}}^{N_I}\mathbf{C}_{i,j}\mathbf{\Phi}_j, \quad i = 1, \ldots, N_I, \tag{55}$$

where $\mathbf{A}_i$, $\mathbf{\Phi}_i$, and $\mathbf{B}_i$ denote the coefficient matrix, unknown potentials, and the known right-hand-side term corresponding to the ith ice floe, respectively; $\mathbf{C}_{i,j}$ denotes the coupling matrix between the ith and jth ice floes caused by Eq. (27). To solve Eq. (55), we may first obtain the solution for each ice floe on its own, or ignore the effects from others, and write the solution as $\mathbf{\Phi}_i^{(0)}$. After that, we may iterate the solution following a procedure similar to the successive overrelaxation (SOR) method, or

$$\mathbf{A}_i\mathbf{\Phi}_i^{(n+1)} = \mathbf{B}_i - \sum_{\substack{j=1\\ j\neq i}}^{N_I}\mathbf{C}_{i,j}\left[\varpi\,\mathbf{\Phi}_j^{(n)} + (1-\varpi)\mathbf{\Phi}_j^{(n-1)}\right], \quad i = 1, 2, \ldots, N_I, \tag{56}$$

where $0 < \varpi \leqslant 1$ denotes the relaxation parameter, which is introduced to balance numerical stability and convergence speed. Specifically, $\varpi = 1$ is used at $n = 1$, and a value $\varpi < 0.5$ is

used at $n \geqslant 2$, depending on the numerical stability and convergence of the case. In addition, the Aitken-accelerated relaxation method [33] can be also employed to dynamically adjust ϖ during the iteration process, which can further improve the convergence speed. Equation (53) has reduced a very large matrix equation to N_I much smaller ones. The solution of $\mathbf{\Phi}_i^{(n+1)}$ only relies on the solution at previous steps, or $\mathbf{\Phi}_j^{(n)}$ and $\mathbf{\Phi}_j^{(n-1)}$ $(j \neq i)$. Each of them may be also solved using the Gauss-Seidel method. Alternatively, as the size of $\mathbf{A}_i$ is much smaller, $\mathbf{A}_i^{-1}$ can be worked out directly and can be used repeatedly for the iteration to account for interaction. This is particularly powerful if all floes are the same and $\mathbf{A}_i^{-1}$ needs to be calculated only once.

Under this framework, the solution for multiple ice floes is effectively simplified to a sequence of single-ice-floe problems. The total stiffness matrix of size $[2(M+3)\sum_{i=1}^{N_I} N_s^{(i)}] \times [2(M+3)\sum_{i=1}^{N_I} N_s^{(i)}]$ is reduced to N_I much smaller matrices of size $[2(M+3)N_s^{(i)}] \times [2(M+3)N_s^{(i)}]$ $(i = 1, \ldots, N_I)$. Moreover, the procedure outlined in Eq. (53) enables parallel computation, allowing the solution for each ice floe to be updated independently, which further improves the efficiency of the computation. The iteration will be truncated at a given error limit. When it is taken to be sufficiently low, the solution will be consistent with that solved by other approaches, e.g., by Gaussian elimination and LU decomposition.

We note that only the mode $m = 0$ corresponds to the traveling wave, while terms of $m \neq 0$ represent evanescent waves, which decay exponentially. Therefore, in Eq. (55), while we keep all the $m = 0$ terms on the right-hand side, the $m > 0$ terms will be kept only when they are still within the desired accuracy. This avoids all the unnecessary computations which would require more effort than the $m = 0$ terms.

IV. NUMERICAL RESULTS AND DISCUSSION

In the following numerical computation, the typical parameters for ice floes are chosen as in Ref. [34], or

$$E_i = 6 \text{ GPa}, \quad \nu_i = 0.3, \quad \rho_i = 922.5 \text{ kg/m}^3, \quad i = 1, \ldots, N_I. \tag{57}$$

All the ice sheets are assumed to have identical thickness $h_i = 1$ m $(i = 1, \ldots, N_I)$. The density of water, $\rho = 1025$ kg/m^3, water depth $H = 20$ m, and acceleration due to gravity, $g = 9.8$ m/s^2, are used in the computation. All the numerical results are presented in nondimensionalised forms based on ρ, g, and a characteristic length.

A. Validation of the numerical approach through a single ice floe

We may first consider the case of an incident wave interacting with a single circular ice floe to validate the numerical method, where the radius $a = 25$ m is used. A comparison is made with the results obtained from a semianalytical method [5]. Here, the perimeter of the ice floe is divided into $N_s^{(1)} = 128$ elements, and the vertical modes in Eqs. (16) and (24) are both truncated at $M = 25$, which has been found to provide the converged results from this case. The vertical force F_z and the scattering cross section $\mathcal{F}$ versus the nondimensionalized wave number $k_0 a$ are shown in Fig. 2. A very good agreement between the present numerical and the analytical results can be observed. Furthermore, in Fig. 2(a), Eqs. (40) and (48) provide the graphically indistinguishable results for the hydrodynamic forces. Similarly, Fig. 2(b) shows the graphically indistinguishable results of the scattering cross section obtained using Eqs. (52) and (53).

B. Wave interaction with a long array of circular ice floes

A case study is conducted first for wave interaction with an array of identical floating circular ice floes, as sketched in Fig. 3, where the distance between the centers of each of two adjacent ice floes is $d = 2a$. To ensure that $N_s^{(1)} = 128$ and $M = 25$ also give converged results for multiple floes, a calculation is performed for $N_I = 4$ circular ice floes with a radius of $a = 25$ m, and the incident

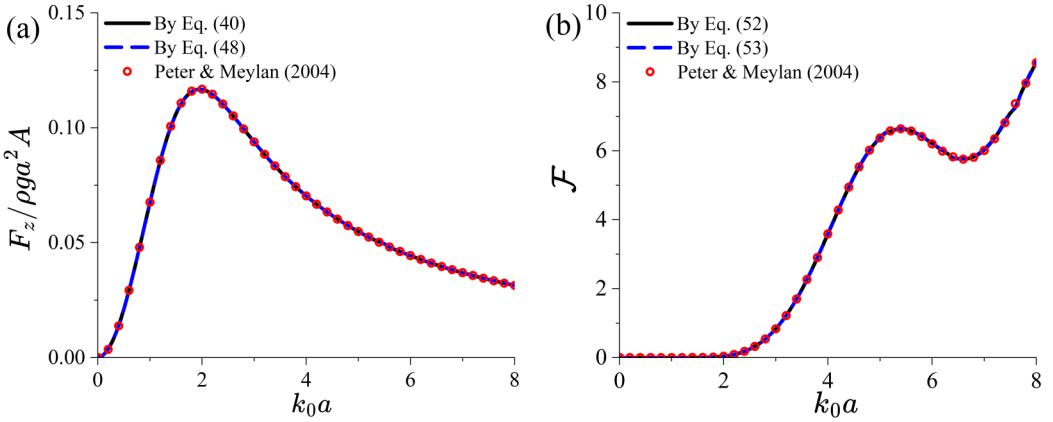

FIG. 2. A comparison between the present results and the semianalytical solution for a single circular ice floe: (a) Vertical wave force and (b) Scattering cross section ($H/a = 0.8$, $h_i/a = 0.04$).

wave angle is selected to be $\beta = \pi/2$. The Gaussian elimination with pivot selection is used to avoid inaccuracy from other sources when the study is undertaken. The vertical forces on the first and second ice floes, as well as the scattering cross section, are shown in Fig. 4. A good agreement between the results from $N_s^{(i)} = 128$ and $M = 25$ ($i = 1, \ldots, 4$) and from $N_s^{(i)} = 256$ and $M = 50$ can be seen. In the following, $N_s^{(i)} = 128$ and $M = 25$ ($i = 1, \ldots, N_I$) are adopted.

For the case shown in Fig. 4, we further compare the solution obtained using the above Gaussian elimination method with that obtained from the approach in Sec. III F. When using the Gaussian elimination, every term in the system of linear equations in Eqs. (36)–(38) is kept. By contrast, when using the approach in Sec. III F, in Eq. (27), for $m = 1, 2, \ldots$, the coupling terms from other ice floes are ignored if $e^{-2ik_m d} < \varepsilon = 10^{-5}$, since the corresponding evanescent wave component is almost virtually diminished when propagating from one ice floe to the adjacent one. When the number of iterations $N_T = 1$, Figs. 5(a) and 5(c) indicate that the exact numerical solution and the one obtained using the approach in Sec. III F exhibit only slight differences in the vertical force F_z on the second ice floe and the scattering cross section $\mathcal{F}$. By contrast, for the roll moment M_x in Fig. 5(b), no visible difference is observed. When N_T is increased to 4, F_z and $\mathcal{F}$ from the iteration method show very good agreement with the exact numerical results. A similar study is also conducted for the case of incident wave angle $\beta = 0$, and the results are shown in Fig. 6. When $N_T = 1$, significant differences are observed in F_z, M_y on the fourth ice floe, and $\mathcal{F}$. However, when $N_T = 4$, very good agreement is achieved for all three physical variables. Figures 5 and 6 show that the proposed method can provide accurate results even when N_T is relatively small. In other cases, a larger N_T may be needed. However, the number of operations is still significantly lower than that of the solution of a full matrix, especially when the evanescent wave components are avoided.

We now use the approach proposed in Sec. III F to conduct a study for arrays of different numbers of ice floes. The computation is terminated when the condition $\max_{i=1,\ldots,N_I} \|\mathbf{\Phi}_i^{(n+1)} - \mathbf{\Phi}_i^{(n)}\|_\infty < \epsilon = 10^{-2}$ is satisfied, as the results smaller than this do not affect the curve graphically. Correspondingly, the effect of the evanescent wave component is ignored when $e^{-2ik_m d} < \varepsilon = 10^{-5}$. It

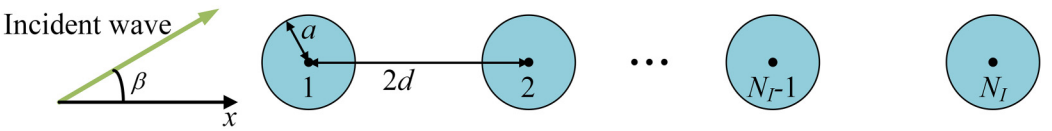

FIG. 3. A sketch of wave interaction with a long array of circular ice floes.

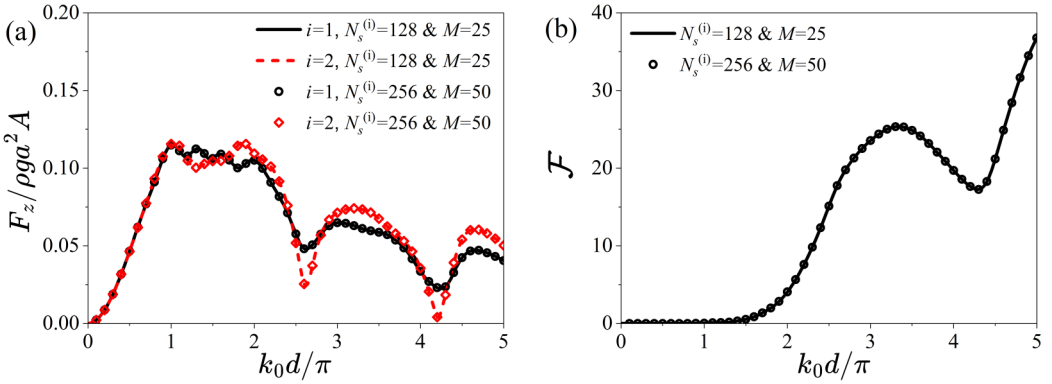

FIG. 4. Mesh convergence test for an array of four circular ice floes in the incident wave of angle $\beta = \pi/2$: (a) Vertical wave force and (b) Scattering cross section ($H/a = 0.8$, $h_i/a = 0.04$, $d/a = 2$).

should be noted that $\epsilon = 10^{-2}$ here is to control the accuracy of the final solution, while $\varepsilon = 10^{-5}$ is used to check the magnitude of the coefficients in the system of linear equations.

Figure 7 presents the hydrodynamic forces on the middle ice floe in an array subjected to an incident wave with $\beta = \pi/2$. The results for $N_I = 1, 3, 19$ together with a single ice floe in the channel from Ref. [22] are provided. In Fig. 7(a), for long waves when $k_0 d/\pi < 0.9$, there is hardly any visible difference in F_z among all four cases. As k_0 increases, F_z exhibits a fluctuating trend with respect to $k_0 d/\pi$ in cases of multiple ice floes, evidently different from the single-ice-floe case. However, for the case of $N_I = 3$ and 19, F_z on the middle ice floe differs only slightly. It is worth noting that when the number of ice floes, N_I, is sufficiently large, F_z is expected to tend to that of a single ice floe at the center of a free-surface channel with width $B = 2d$. This similarity arises because the two sidewalls of the channel act like mirrors, making the channel case equivalent to that of an infinite array of ice floes. It can therefore be seen that when $N_I = 19$, the result is close to that of Ref. [22]. For the moment M_x, Fig. 7(b) shows that the results tend to that of channel one very quickly, and those of $N_I = 3, 19$ and the free-surface channel are very close. Relative to F_z, the result of M_x does not have strong fluctuation. It should be mentioned that in Ref. [22] only the hydrodynamic forces induced by the ϕ component in Eq. (40) are included. As a result, $F_z \to \rho g S A$ as $k_0 \to 0$, where S denotes the area of the ice floe. Here, both components in Eq. (40) are included, leading to $F_z \to 0$ when $k_0 \to 0$. For the case of $N_I = 19$, the hydrodynamic forces on the $i = 1, 5$,

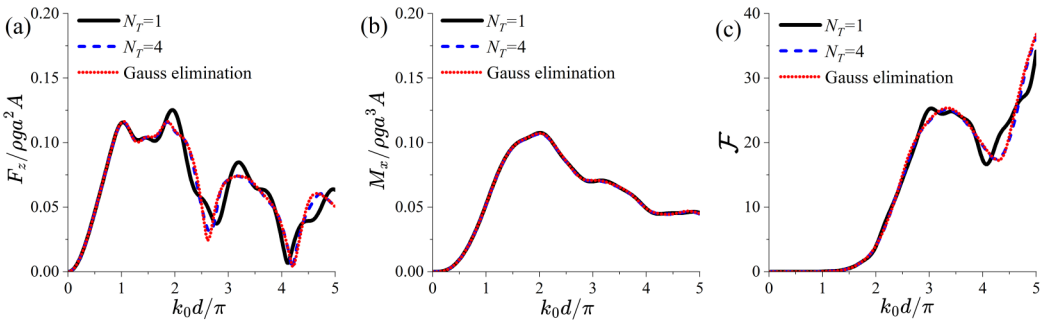

FIG. 5. Comparison between the solution by the Gauss elimination method and the iterative approach for an array of four circular ice floes in an incident wave angle of $\beta = \pi/2$: (a) Vertical wave force on the second ice floe, (b) Roll moment on the second ice floe, and (c) Scattering cross section ($H/a = 0.4$, $h_i/a = 0.04$, $d/a = 2$).

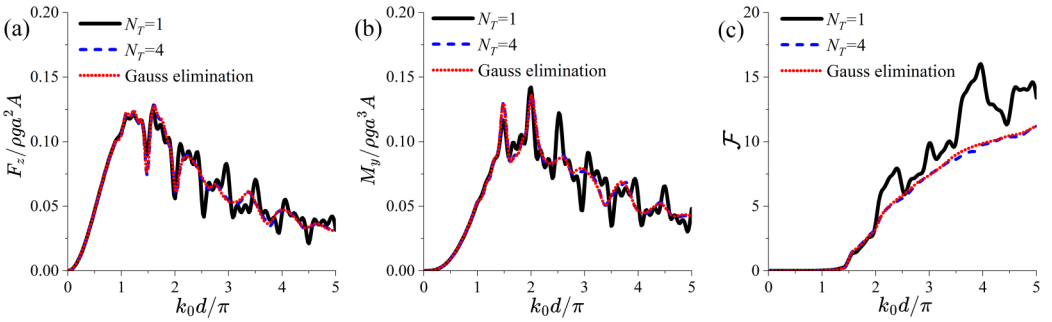

FIG. 6. Comparison between the solution by the Gauss elimination method and the iterative approach for an array of four circular ice floes under an incident wave angle of $\beta = 0$: (a) Vertical wave force on the fourth ice floe, (b) Pitch moment on the fourth ice floe, and (c) Scattering cross section ($H/a = 0.4$, $h_i/a = 0.04$, $d/a = 2$).

and 10 ice floes are presented in Fig. 8. In Fig. 8(a), F_z on the first floe shows some small difference from those on the fifth and tenth floes. Figure 8(b) indicates that M_x for all three floes are nearly identical across the entire wave number range.

We also consider wave interaction with an array of ice floes under an incident wave angle $\beta = 0$. The hydrodynamic forces versus the wave number on the last ice floe are plotted in Fig. 9, where $N_I = 5$, 19, and 49 are considered. It can be found that both F_z and M_y oscillate around the result of the corresponding single floe, while the results of the three multifloe cases exhibit very similar variation trends. This is because, as N_I increases, the effect of the wave field created by the floes near the front diminishes toward the tail of the array. Additionally, when $k_0 d/\pi$ is close to 1.5 and 2, two obvious troughs can be observed in the curves of F_z in Fig. 9(a), whereas M_y in Fig. 9(b) shows distinct peaks. We may further take $N_I = 49$ as an example to analyze the forces on other ice floes. In particular, F_z and M_y on the $i = 1$, 25, and 49 ice floes are plotted in Fig. 10. When $k_0 d/\pi < 1$, it can be seen that F_z and M_y on all three floes are nearly the same and are close to those of a single ice floe. This can be linked to natural frequencies $k_0 2d/\pi = n$ of the channel problem (e.g., Refs. [35,36]). When $\beta = \pi/2$, for the 25th ice floe, the middle vertical surfaces between the 25th and the 24th, as well as between the 25th and the 26th, act like mirrors, and other floes

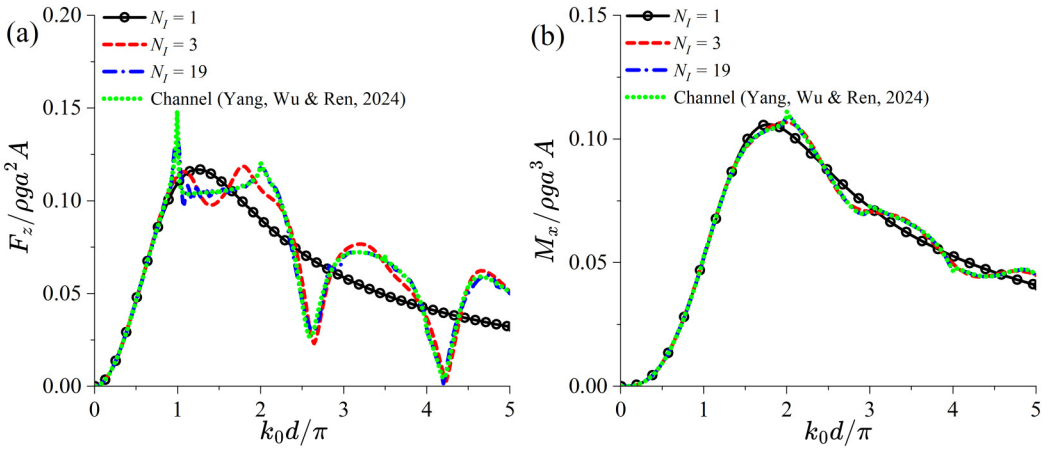

FIG. 7. Hydrodynamic forces on the middle one in arrays of different numbers of circular ice floes: (a) Vertical wave force and (b) Roll moment ($\beta = \pi/2$, $H/a = 0.8$,$h_i/a = 0.04$, $d/a = 2$).

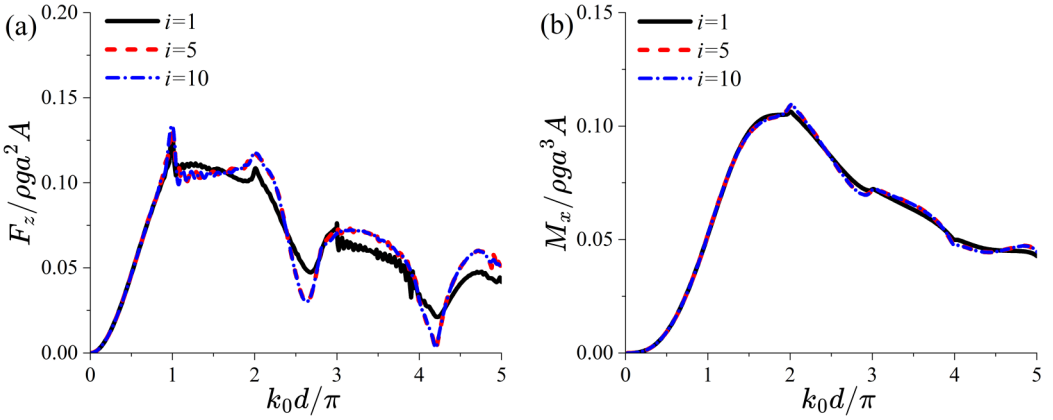

FIG. 8. Hydrodynamic forces on different floes in an array of $N_I = 19$ circular ice floes: (a) Vertical wave force and (b) Roll moment ($\beta = \pi/2$, $H/a = 0.8$, $h_i/a = 0.04$, $d/a = 2$).

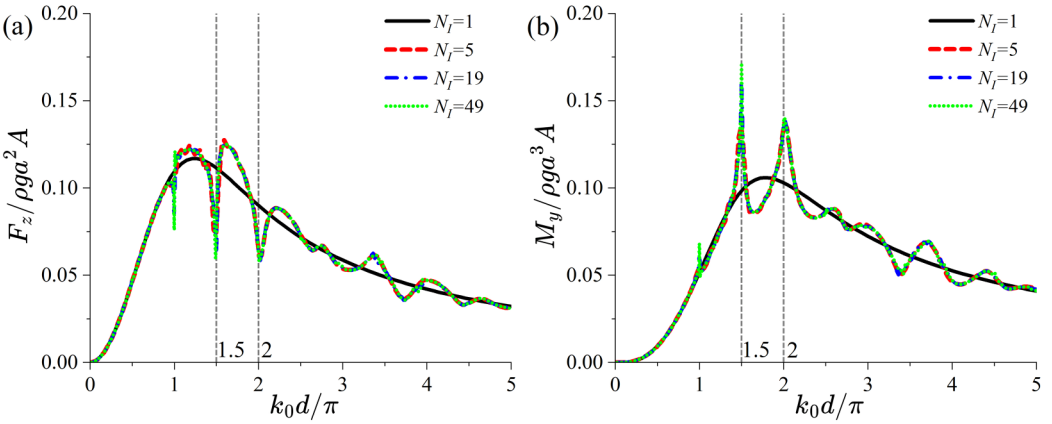

FIG. 9. Hydrodynamic forces on the last floe of arrays of different numbers of circular ice floes: (a) Vertical wave force and (b) Pitch moment ($\beta = 0$, $H/a = 0.8$, $h_i/a = 0.04$, $d/a = 2$).

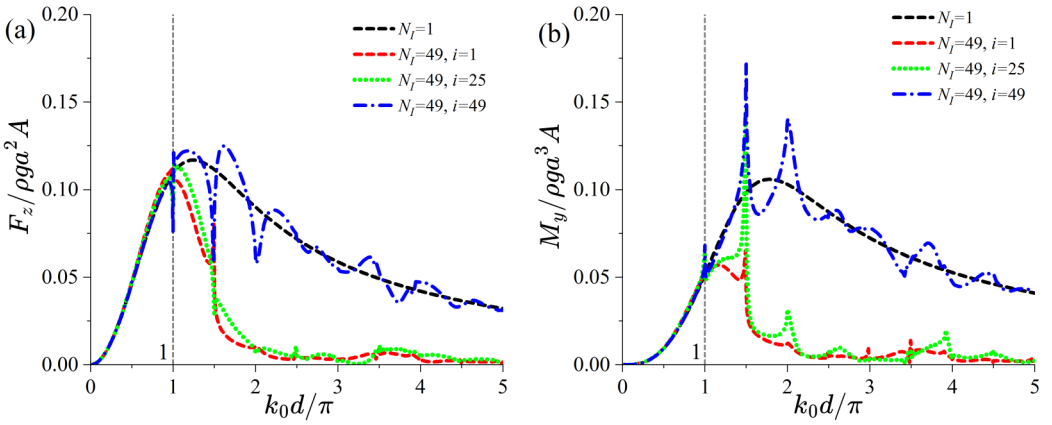

FIG. 10. Hydrodynamic forces on different floes in an array of $N_I = 49$ circular ice floes: (a) Vertical wave force and (b) Pitch moment ($\beta = 0$, $H/a = 0.8$, $h_i/a = 0.04$, $d/a = 2$).

act like successive mirror images. When the number of images is infinite, this in fact becomes a channel problem. The problem is symmetric, and there will be only even modes corresponding to even n present. When there are 24 mirror images on each side, the channel solution can be a good approximation. As shown by Ref. [37], the effect of a given natural frequency will be activated only when the wave frequency is larger than this natural frequency. A similar phenomenon was also reported by Ref. [38] for wave scattering by a metacylinder in a channel, where the result exhibits a rapid change as $k_0 d/\pi$ passes through 1. Here, when the wave frequency is lower than all the natural frequencies, the effect of the channel is small, and the results are close to those of a single floe in the open water, or the effect of the number of mirror images on the middle flow is small.

For $\beta = 0$, or when the wave is along the array, when $2k_0 d/\pi = 1$, the incident wave from one floe to the next will have a phase shift of $\pm\pi$. When $2k_0 d/\pi = 2$, the incident wave will have the same effect on each floe, which is similar to a channel problem. When $k_0 d/\pi > 1$, the difference between the results for different floes becomes obvious. F_z and M_y on the 1st and 25th ice floes are generally smaller than those on the 19th floe and in the single-ice-floe case, except at several peak points. Moreover, in Fig. 10(b), near $k_0 d/\pi = 1.5$, very obvious peaks of M_y can be observed on the 1st and 25th ice floes. However, it should be pointed out that although these peaks on different ice floes may appear to occur at the same wave number, the numerical results in fact are not exactly the same. The peak values of the 1st and 25th ice floes occur at $k_0 d/\pi \approx 1.49$ with $M_y/\rho g a^3 A \approx 0.0653$ and 0.1434, respectively, while the peak for the 49th occurs at $k_0 d/\pi \approx 1.50$ with $M_y/\rho g a^3 A \approx 0.1717$.

Figure 11 shows the distribution of the vertical wave force and pitch moment along an array of $N_I = 49$ ice floes for $k_0 d/\pi = 1.49$, 1.50, and 1.51. It is worth noting that at $k_0 d/\pi = 1.50$, the incident wave of $\beta = 0$ has a phase shift $\pm\pi$ from the one floe to the next, or the phases of two adjacent floes are completely opposite to each other. At $k_0 d/\pi = 1.49$ and 1.51, the phase shift moves in a different direction. It can be seen that the distributions of F_z and M_y change significantly, although the variation of $\Delta k_0 d/\pi$ is only 0.01. At $k_0 d/\pi = 1.49$, the maximum values of F_z and M_y occur on the 1st and 19th ice floe, respectively. By contrast, at $k_0 d/\pi = 1.50$ and 1.51, the maximum values of F_z and M_y both occur on the last ice floe. In addition to the case of $N_I = 49$, we also consider a larger array with $N_I = 100$, as shown in Fig. 12, where a similar variation trend and phenomena can be observed. It is worth noting that the rapid changes in hydrodynamic force distributions caused by small variations in wave number are similar to the behavior reported for long arrays of vertical circular cylinders by Maniar and Newman [39].

Apart from the hydrodynamic forces, we may also investigate the diffracted wave energy to illustrate the disturbance of waves by the structures. The scattered cross section $\mathcal{F}$ against wave number for the case of $N_I = 19$ is plotted in Fig. 13 as an example. The results from Eqs. (52) and (53) show a good agreement, which has further confirmed the accuracy of the iteration procedure in Sec. III F. For the case of $\beta = \pi/2$, a maximum can be found around $k_0 d/\pi = 3.34$, while a trough appears at $k_0 d/\pi = 4.28$, while the variation near these points is mild. For the case of $\beta = 0$, a rapid change can be observed near $k_0 d/\pi = 1.5$, which corresponds to the pronounced peak (trough) value in M_y (F_z) in Fig. 9. This phenomenon is associated with the phase shift of the incident wave, as discussed above. Moreover, the magnitude of $\mathcal{F}$ for the case $\beta = \pi/2$ is normally much larger than that of $\beta = 0$. We may further present contour plots of the modulus of the diffraction coefficient $|U|$ versus θ and $k_0 d/\pi$ for the cases of $\beta = \pi/2$ and $\beta = 0$. The results in Fig. 14 show that the incident wave angle significantly affects the spatial distribution of the diffracted wave energy, including the peak positions at a given value of k_0.

C. Wave interaction with one or two long arrays of elliptical ice floes

The approach in this paper is applicable to ice floes of arbitrary shapes. Here, we may further consider cases of single and double arrays of elliptical ice floes, as sketched in Fig. 15, where all the ice floes are still assumed to be identical. The major and minor axes of each ice floe are denoted by r_y and r_x, respectively. We may define $\gamma = \gamma_y/\gamma_x$, and let $r_x r_y = a^2 = 625\ \mathrm{m}^2$, so the area of

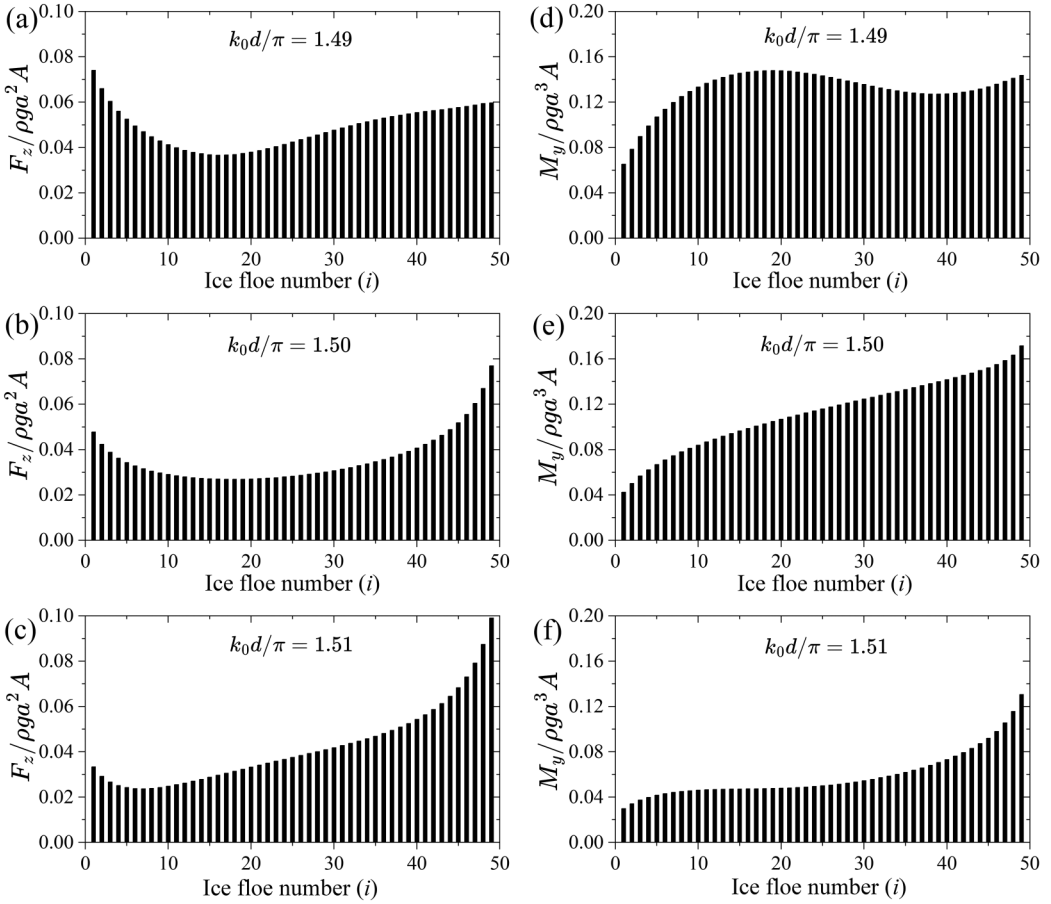

FIG. 11. The distribution of the hydrodynamic forces along the array of 49 circular ice floes at different wave numbers: [(a)–(c)] Vertical forces and [(b)–(d)] Pitch moment ($\beta = 0$, $H/a = 0.8$, $h_i/a = 0.04$, $d/a = 2$).

the ellipse is the same as that of the circle considered previously. The distance between each of two adjacent ice floes is also set to be $d = 2a$.

We first consider water waves with incident angle $\beta = 0$ interacting with an array of $N_I = 19$ elliptical ice floes, as sketched in Fig. 15(a). Figure 16 shows F_z and M_y on the 19th ice floe at aspect ratios $\gamma = 1.0$, 1.5, and 2.0. In Figs. 16(a) and 16(b), when k_0d/π is near $n/2$ ($n = 3, 4, 5, \ldots$), F_z and M_y vary relatively rapidly, and evident troughs in F_z and peaks in M_y can be observed, respectively. The corresponding physical mechanism is quite similar to the circular ice floe case described in Fig. 9. In addition, for different γ, the wave numbers corresponding to these peaks are close but not identical. Furthermore, in Fig. 16(a), at a fixed value of k_0, except when k_0 is very small or near values leading to troughs, F_z is generally largest at $\gamma = 2.0$, followed by that at $\gamma = 1.5$ and then $\gamma = 1.0$. We may further take the case of $N_I = 19$ as an example, F_z and M_y on the 1st, 10th, and 19th ice floes versus k_0d/π are shown in Fig. 17, in which phenomena similar to those in Fig. 9 are also observed.

We may further consider two rows of elliptical ice floes shown in Fig. 15(b). Each row contains 19 ice floes or $N_I = 38$ in total, and the gap between the two rows is $B = 4d$. We may consider two cases, with $l = 0, d$, respectively, where the definition of l is shown in Fig. 15. The hydrodynamic forces on the last ice floe of each row, $N_I = 19$ and $N_I = 38$, respectively, for an incident wave of

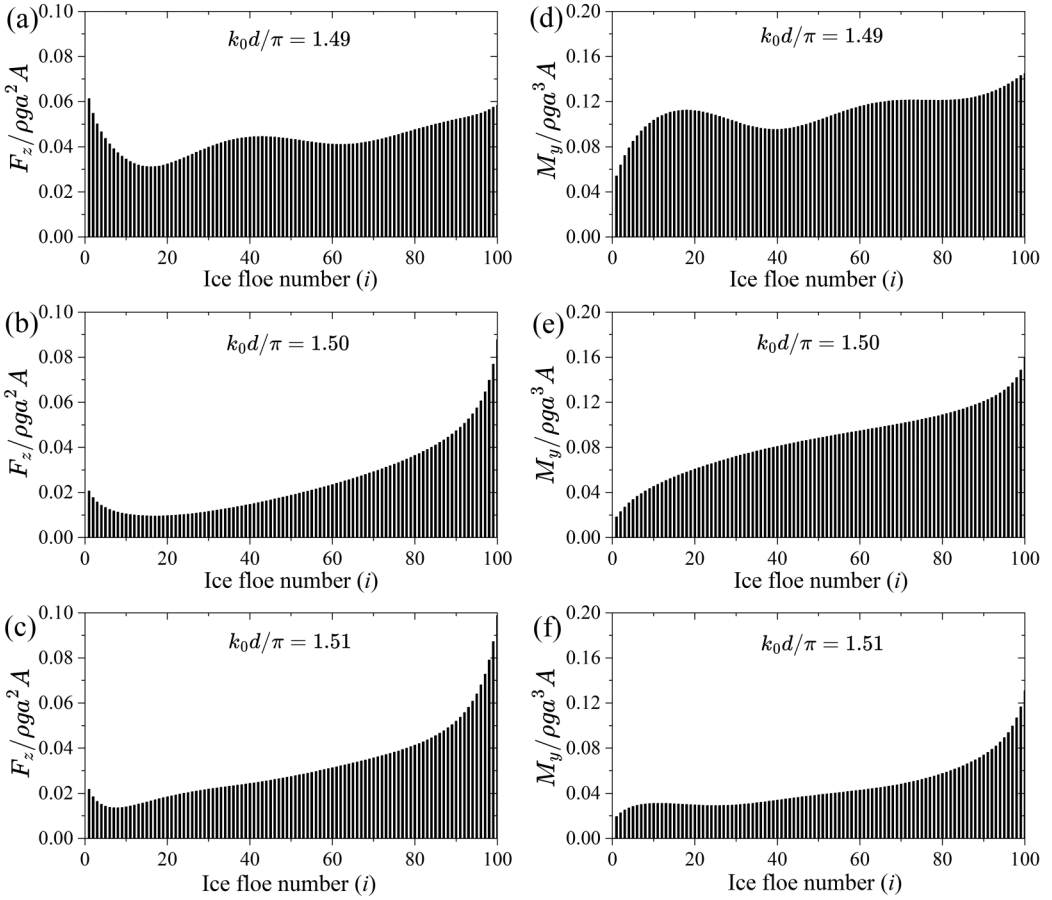

FIG. 12. The distribution of the hydrodynamic forces along the array of 100 circular ice floes at different wave numbers: [(a)–(c)] Vertical forces and [(b)–(d)] Pitch moment ($\beta = 0$, $H/a = 0.8$, $h_i/a = 0.04$, $d/a = 2$).

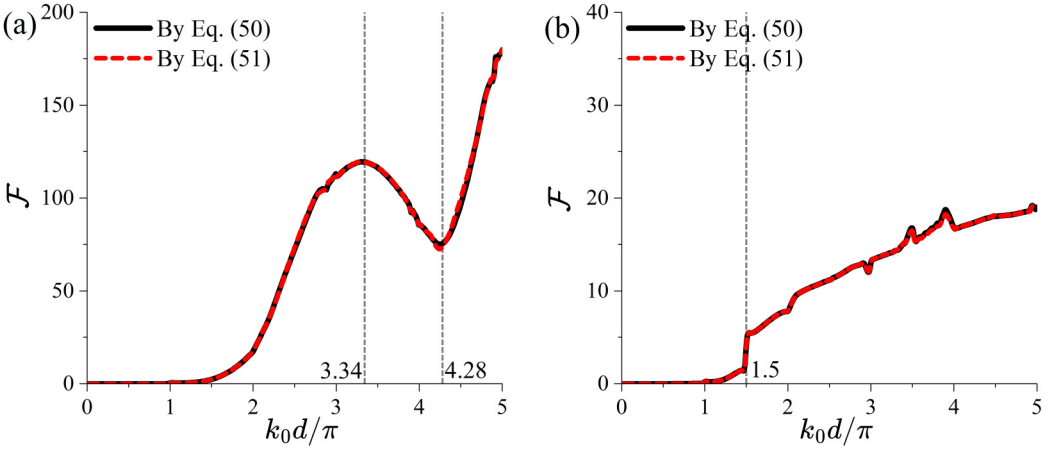

FIG. 13. The scattered cross section $\mathcal{F}$ due to an array of $N_I = 19$ circular ice floes: (a) Incident wave angle $\beta = \pi/2$ and (b) Incident wave angle $\beta = 0$ ($H/a = 0.8$, $h_i/a = 0.04$, $d/a = 2$).

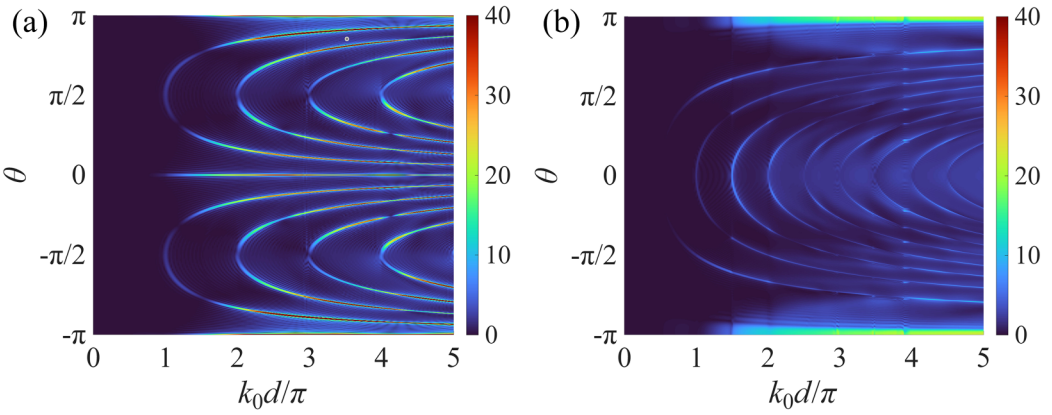

FIG. 14. Modulus of the diffraction coefficient $|U|$ as a function of θ and wave number for the case of $N_I = 19$: (a) Incident wave angle $\beta = \pi/2$ and (b) Incident wave angle $\beta = 0$ ($H/a = 0.8$, $h_i/a = 0.04$, $d/a = 2$).

$\beta = 0$ are shown in Fig. 18. It should be noted that in case 1, the forces on the first and second rows are identical due to the symmetry of the configuration. It can be found that the variation trends of F_z and M_y in these two cases generally follow those of the single row of $N_I = 19$ ice floes. However, as a result of the interaction of the two rows of ice floes, some local oscillations can be found in the curves of F_z and M_y. In Figs. 18(a) and 18(b), it can be also observed that the most pronounced trough (peak) occurs at F_z (M_y) around $k_0\pi/d = 2.0$. Hence, we may take this as a case of the distribution of F_z and M_y along each row of ice floes and the results are shown in Fig. 19. Here, the horizontal axis denotes the floe number, starting from the first floe in each row. It can be found that both the maximum values of F_z and M_y occur at the last ice floes.

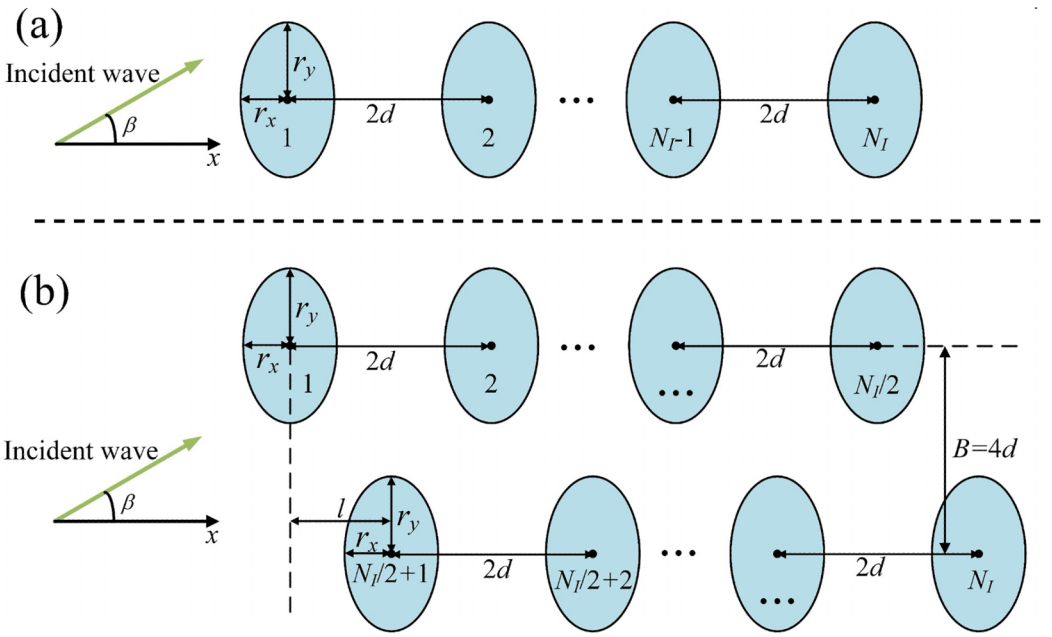

FIG. 15. A sketch of wave interaction with single and double arrays of elliptical ice floes.

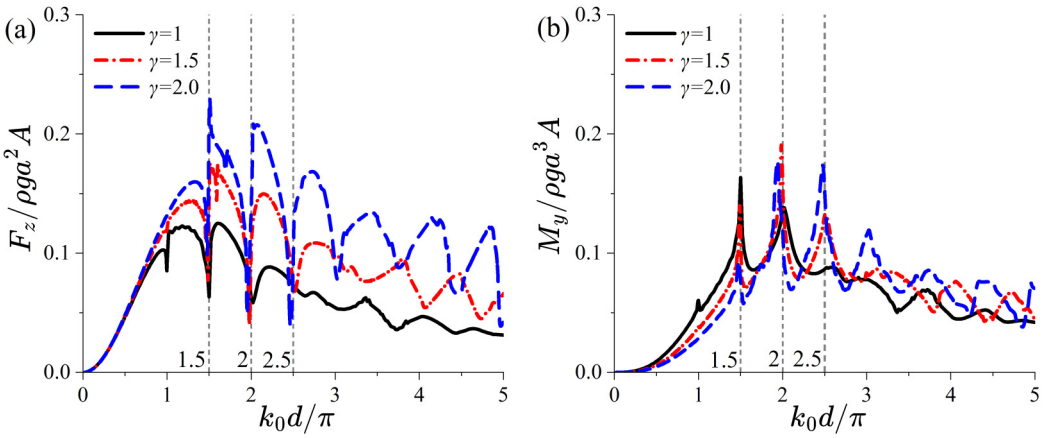

FIG. 16. Hydrodynamic forces on the 19th ice floe in an array of 19 elliptical floes of different aspect ratios: (a) Vertical wave force and (b) Pitch moment ($\beta = 0$, $H/a = 0.8$, $h_i/a = 0.04$, $d/a = 2$).

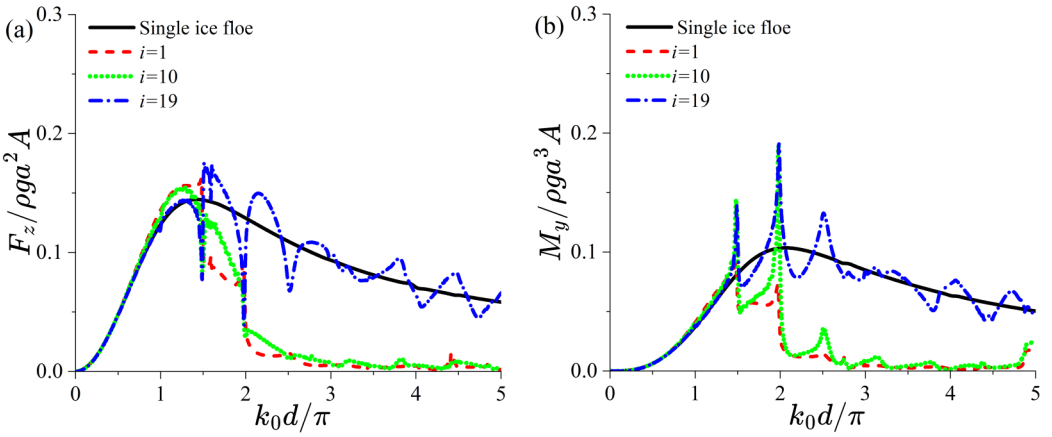

FIG. 17. Hydrodynamic forces on different floes in an array of $N_I = 19$ elliptical ice floes: (a) Vertical wave force and (b) Pitch moment ($\beta = 0$, $H/a = 0.8$, $h_i/a = 0.04$, $d/a = 2$).

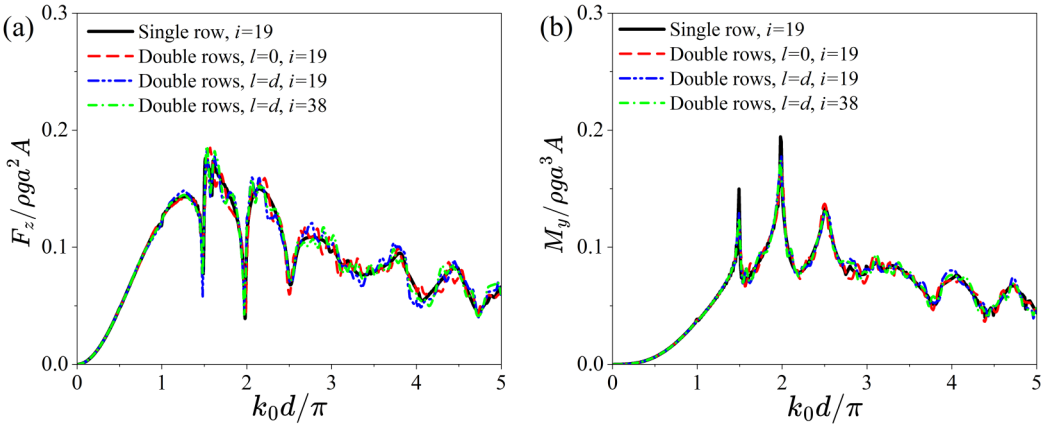

FIG. 18. Hydrodynamic forces on the last floe in each row of two arrays of 38 elliptical ice floes: (a) Vertical wave force and (b) Pitch moment ($\beta = 0$, $H/a = 0.8$, $h_i/a = 0.04$, $d/a = 2$).

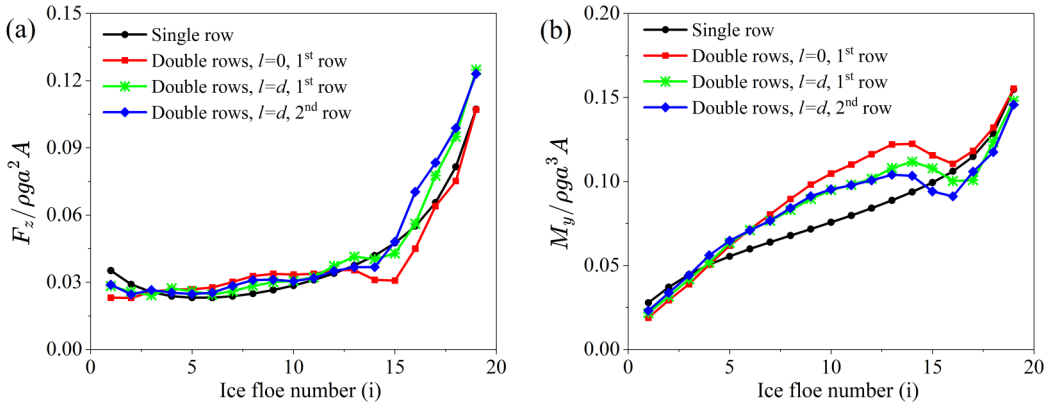

FIG. 19. Hydrodynamic force distribution along each row of elliptical ice floes at $k_0 d/\pi = 2.0$ ($\beta = 0$, $H/a = 0.8$, $h_i/a = 0.04$, $d/a = 2$, $B/a = 8$, $\gamma = 1.5$).

V. CONCLUSION

The problem of water wave interaction with a large array of ice floes of arbitrary shapes and arrangements is studied in this paper. The entire fluid domain is divided into free-surface and ice-covered subdomains. In each subdomain, the velocity potential is constructed using the boundary integral equation, together with the Green's function satisfying the free-surface or ice sheet conditions. The 3D problem is subsequently reduced to an infinite set of 2D problems. The unknowns will be the 2D potentials and normal velocities in the vertical mode expansion on the interface of two domains. They are obtained through imposing the continuity conditions at the interface, together with the zero bending moment and shear force conditions at the free ice edges. To reduce computational cost when the number of ice floes becomes very large, an efficient iterative method is adopted, and the evanescent wave is ignored when it does not affect the desired accuracy. This is verified through convergence study and comparison with the published results.

The procedure here can be used for ice floes of arbitrary shape and distribution. Calculation is first conducted for a long array of circular ice floes with identical geometry and uniform spacing. When the direction of the incident wave is perpendicular to the direction of the ice floe array ($\beta = \pi/2$), it is confirmed that the hydrodynamic forces on the middle ice floe gradually approach those of an ice floe floating in a channel as the number of floes increases. Compared with the case of a single ice floe, the vertical force F_z shows an oscillatory behavior against the wave number, whereas the moment M_x remains similar and varies smoothly. When the direction of the incident wave is parallel to the direction of the ice floe array ($\beta = 0$), the incident wave will have a phase shift when propagating from one ice floe to another. In particular, when $k_0 d/\pi > 1$, the difference between the results for different floes becomes obvious. When $k_0 d/\pi$ is close to $n/2$, where n is an integer (e.g., $n = 3, 4, \ldots$), Pronounced peaks (troughs) can be observed in the curves of M_y (F_z). Although the wave numbers leading to these peaks (troughs) for different ice floes are close, they are in fact slightly different. Further analysis of the hydrodynamic force distributions along the ice floe array near these wave numbers indicates that they are highly sensitive to wave numbers; even small variations can cause significant changes in the distribution. For the hydrodynamic force on the last ice floe, F_z and M_y oscillate around the results of a single ice floe. As the number of ice floes increases, the effect of the wave field created by the floes near the front diminishes toward the tail of the array. When the array becomes sufficiently large, the curves of F_z and M_y no longer change, tending to a stable limit.

Calculations are also made for single and double arrays of elliptical floes under the incident wave angle $\beta = 0$, as examples for floes of other geometries. Similar to the results in circular ice floe arrays, peaks and troughs are found on the curves of M_y and F_z. However, the magnitude of these

peak or trough values, as well as their corresponding wave frequency, is related to the geometry and configuration of the ice floes.

ACKNOWLEDGMENTS

Y.F.Y. gratefully acknowledges support for this work from the NERC Arctic Office under the grant "Supporting Impactful UK Arctic Science Engagement 2025–2026." The computations in this paper are supported by EPSRC through access to the UK national supercomputing facility ARCHER2 via the HEC-WSI project.

DATA AVAILABILITY

The data that support the findings of this article are not publicly available upon publication because it is not technically feasible and/or the cost of preparing, depositing, and hosting the data would be prohibitive within the terms of this research project. The data are available from the authors upon reasonable request.

[1] D. Dumont, Marginal ice zone dynamics: History, definitions and research perspectives, Philos. Trans. R. Soc. A **380**, 20210253 (2022).
[2] L. C. Smith and S. R. Stephenson, New trans-arctic shipping routes navigable by midcentury, Proc. Natl. Acad. Sci. USA **110**, E1191 (2013).
[3] M. Ewing and A. P. Crary, Propagation of elastic waves in ice, part II, Physics **5**, 181 (1934).
[4] M. H. Meylan and V. A. Squire, Response of a circular ice floe to ocean waves, J. Geophys. Res. **101**, 8869 (1996).
[5] M. A. Peter, M. H. Meylan, and H. Chung, Wave scattering by a circular elastic plate in water of finite depth: A closed form solution, Int. J. Offshore Polar Eng. **14**, 02 (2004).
[6] F. Montiel, L. G. Bennetts, V. A. Squire, F. Bonnefoy, and P. Ferrant, Hydroelastic response of floating elastic discs to regular waves. Part 2. Modal analysis, J. Fluid Mech. **723**, 629 (2013).
[7] M. H. Meylan and L. G. Bennetts, Three-dimensional time-domain scattering of waves in the marginal ice zone, Philos. Trans. R. Soc. A **376**, 20170334 (2018).
[8] R. Porter, The coupling between ocean waves and rectangular ice sheets, J. Fluids Struct. **84**, 171 (2019).
[9] K. Ren, G. X. Wu, and Y. F. Yang, Surface wave interaction with floating elastic plates in channels, Phys. Fluids **36**, 017143 (2024).
[10] M. H. Meylan, Wave response of an ice floe of arbitrary geometry, J. Geophys. Res. **107**, 5 (2002).
[11] J. V. Wehausen and E. V. Laitone, *Fluid Dynamics/Strömungsmechanik* (Springer, Berlin, 1960), p. 446.
[12] C. D. Wang and M. H. Meylan, A higher-order-coupled boundary element and finite element method for the wave forcing of a floating elastic plate, J. Fluids Struct. **19**, 557 (2004).
[13] L. G. Bennetts and T. D. Williams, Wave scattering by ice floes and polynyas of arbitrary shape, J. Fluid Mech. **662**, 5 (2010).
[14] M. A. Peter and M. H. Meylan, Infinite-depth interaction theory for arbitrary floating bodies applied to wave forcing of ice floes, J. Fluid Mech. **500**, 145 (2004).
[15] L. G. Bennetts and V. A. Squire, Wave scattering by multiple rows of circular ice floes, J. Fluid Mech. **639**, 213 (2009).
[16] F. Montiel, V. Squire, and L. Bennetts, Attenuation and directional spreading of ocean wave spectra in the marginal ice zone, J. Fluid Mech. **790**, 492 (2016).
[17] Y. Y. Shi, Z. F. Li, and G. X. Wu, Interaction of wave with multiple wide polynyas, Phys. Fluids **31**, 067111 (2019).

[18] F. Montiel, M. Meylan, and S. Hawkins, Scattering kernel of an array of floating ice floes: Application to water wave transport in the marginal ice zone, Proc. R. Soc. A **480**, 20230633 (2024).
[19] J. Song, C.-C. Lu, and W. C. Chew, Multilevel fast multipole algorithm for electromagnetic scattering by large complex objects, IEEE Trans. Antennas Propag. **45**, 1488 (1997).
[20] V. A. Squire, Ocean wave interactions with sea ice: A reappraisal, Annu. Rev. Fluid Mech. **52**, 37 (2020).
[21] C. Fox and V. A. Squire, On the oblique reflexion and transmission of ocean waves at shore fast sea ice, Philos. Trans. R. Soc. London Ser. A **347**, 185 (1994).
[22] Y. Yang, G. Wu, and K. Ren, Hydroelastic wave interaction with a circular crack of an ice-cover in a channel, J. Fluids Struct. **130**, 104173 (2024).
[23] D. V. Evans and R. Porter, Wave scattering by narrow cracks in ice sheets floating on water of finite depth, J. Fluid Mech. **484**, 143 (2003).
[24] T. Sahoo, T. L. Yip, and A. T. Chwang, Scattering of surface waves by a semi-infinite floating elastic plate, Phys. Fluids **13**, 3215 (2001).
[25] Z. F. Li, Y. Y. Shi, and G. X. Wu, A hybrid method for linearized wave radiation and diffraction problem by a three dimensional floating structure in a polynya, J. Comput. Phys. **412**, 109445 (2020).
[26] J. V. Wehausen, The wave resistance of ships, Adv. Appl. Mech. **13**, 93 (1973).
[27] C. M. Linton and P. McIver, *Handbook of Mathematical Techniques for Wave/Structure Interactions* (CRC Press, Boca Raton, FL, 2001).
[28] Y. F. Yang, G. X. Wu, and K. Ren, Hydroelastic wave diffraction by a vertical circular cylinder standing in a channel with an ice cover, J. Fluid Mech. **941**, A13 (2022).
[29] C. H. Lu, Y. S. He, and G. X. Wu, Coupled analysis of nonlinear interaction between fluid and structure during impact, J. Fluids Struct. **14**, 127 (2000).
[30] M. N. Özişik, H. R. Orlande, M. J. Colaço, and R. M. Cotta, *Finite Difference Methods in Heat Transfer* (CRC Press, Boca Raton, FL, 2017).
[31] M. Abramowitz and I. A. Stegun, *National Bureau of Standards Applied Mathematics 55* (U.S. Department of Commerce, 1965).
[32] Z. F. Li, G. X. Wu, and Y. Y. Shi, Wave diffraction by a circular crack in an ice sheet floating on water of finite depth, Phys. Fluids **30**, 117103 (2018).
[33] K. E. Atkinson, *An Introduction to Numerical Analysis* (John Wiley & Sons, New York, 2008).
[34] V. A. Squire, J. P. Dugan, P. Wadhams, P. J. Rottier, and A. K. Liu, Of ocean waves and sea ice, Annu. Rev. Fluid Mech. **27**, 115 (1995).
[35] C. M. Linton, D. V. Evans, and F. T. Smith, The radiation and scattering of surface waves by a vertical circular cylinder in a channel, Philos. Trans. R. Soc. London Ser. A **338**, 325 (1992).
[36] G. X. Wu, Wave radiation and diffraction by a submerged sphere in a channel, Q. J. Mech. Appl. Math. **51**, 647 (1998).
[37] Y. F. Yang, G. X. Wu, and K. Ren, Three-dimensional interaction between uniform current and a submerged horizontal cylinder in an ice-covered channel, J. Fluid Mech. **928**, A4 (2021).
[38] H. Liang, R. Porter, and S. M. Zheng, Wave scattering by plate array metacylinders of arbitrary cross-section, J. Fluid Mech. **1001**, A6 (2024).
[39] H. Maniar and J. Newman, Wave diffraction by a long array of cylinders, J. Fluid Mech. **339**, 309 (1997).